Water Science & Technology

Water Science & Technology Vol 88 No 8, 2033 doi: 10.2166/wst.2023.323

Bamboo charcoal fiber bundles loaded MOF-derived magnetic Co/CoO porous polyhedron for efficiently catalytic degradation of tetracyclines hydrochloride

Lanling Dai[a,b], Ce Cui[a,b], Mengyuan Yang[a,b], Shan Jiang[a,b], Jianwu Lan[a,b] and Ronghui Guo[a,b,c,d,*]

[a] College of Biomass Science and Engineering, Sichuan University, Chengdu 610065, China
[b] Yibin Industrial Technology Research Institute of Sichuan University, Yibin, Sichuan, China
[c] Jiangsu Engineering Research Center of Textile Dyeing and Printing for Energy Conservation, Discharge Reduction and Cleaner Production (ERC), Soochow University, Suzhou 215123, China
[d] Key Laboratory of Jiangxi Province for Persistent Pollutants Control and Resources Recycle, Nanchang Hangkong University, Jiangxi, China
*Corresponding author. E-mail: ronghuiguo214@126.com

RG, 0000-0003-3938-2221

ABSTRACT

The health of living things and the ecosystem of the planet have both been negatively impacted by antibiotic residue in the water environment. There has been a lot of interest in the catalyst made of metal-carbon compounds from MOFs as a potential solution for activating peroxymonosulfate (PMS) to produce reactive oxygen species to catalyze the degradation of residual antibiotics. In this study, zeolitic imidazolate frameworks (ZIF-67) on bamboo fiber bundles (BFB) were pyrolyzed to produce magnetic Co/CoO nanoparticles with porous polyhedrons mounted on bamboo charcoal fiber bundles (BCFB)(BCFB@PCo/CoO). Specific surface area of obtained BCFB@PCo/CoO with abundant active sites arrives at 302.41 m2/g. The catalytic degradation efficiency of Tetracycline hydrochloride (TCH), a target contaminant, could reach up to 99.94% within 15 minutes (PMS = 0.4g/L, Cat. = 0.2g/L). The effects of potential factors, including PMS dosage, interference ions, and temperature, on catalytic degradation efficiencies were investigated. Magnetic recovery and antimicrobial properties of the BCFB@PCo/CoO were also evaluated and the possible degradation pathways were explored. Catalytic mechanism explorations of BCFB@PCo/CoO/PMS system reveal MOF-derived magnetic Co/CoO nanoparticles embedded in BCFB promote the synergistic interaction of both radicals and non-radical pathways for catalytic degradation of TCH. The novel BCFB@PCo/CoO provides an alternative to deal with wastewater containing antibiotics.

Key words: bamboo charcoal fiber bundles, catalytic degradation, Co/CoO nanoparticles, peroxymonosulfate, tetracycline hydrochloride, ZIF-67

HIGHLIGHTS

- A novel BCFB@PCo/CoO catalyst was prepared via in-situ growth and pyrolysis of ZIF-67-coated bamboo fiber bundles.
- The BCFB@PCo/CoO composite exhibits a high catalytic activity (99.94% for 30mg/L TCH within 15 min) and stability.
- The synergistic interaction of both radicals and nonradical pathways for the catalytic degradation of TCH.

GRAPHICAL ABSTRACT

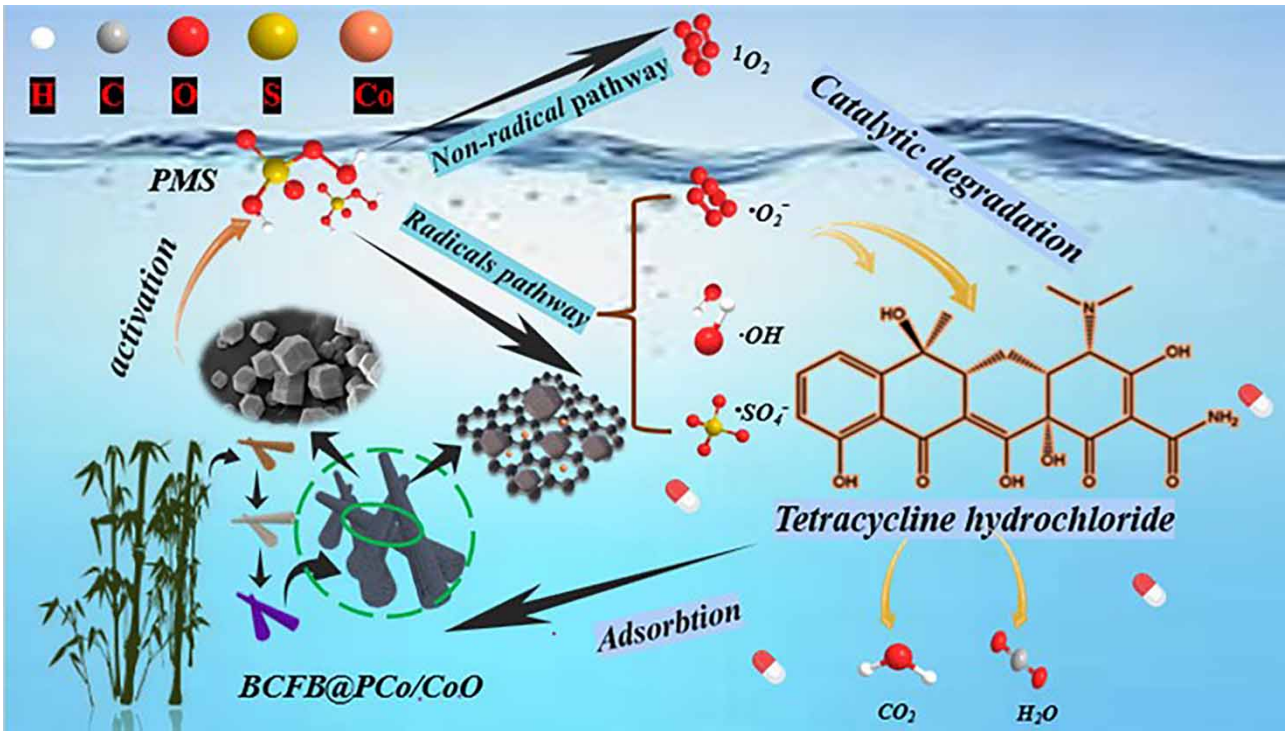

1. INTRODUCTION

With the development of modern society, environmental pollution has attracted more and more attention from society (Daghrir & Drogui 2013; Hu *et al.* 2019; Zhao *et al.* 2022). In recent decades, tetracycline hydrochloride (TCH) has been extensively utilized to deal with animal and human diseases, or as an additive to promote the rapid growth of poultries and aquatic animals or plants (Yang *et al.* 2018; Zhang *et al.* 2022c). It was reported that TCH has the following characteristics: high solubility, stable chemical structure, and non-biodegradable (Daghrir & Drogui 2013; Xu *et al.* 2022). High concentrations of TCH were detected in different water systems such as wastewater, groundwater, and surface water (Xu *et al.* 2020). However, the dissolution and metabolism of TCH in the environment cause a serious threat to the human body.

Until now, many technologies have been developed to effectively control and degrade TCH pollutants, including adsorption, biodegradation, catalytic oxidation exchange, membrane filtration, ozonation, and electrolysis (Lv *et al.* 2020). Generally speaking, advanced oxidation processes (AOPs) (Peng *et al.* 2021; Cai *et al.* 2022) have the advantages of simple and convenient operation, environment-friendly, pollution-free, and a high catalytic degradation efficiency. Oxidatively active species (reactive oxygen species, ROS) can be produced in AOPs to effectively destroy the stable chemical structure of organic pollutants and prompt them to mineralize into CO_2 and H_2O (Duan *et al.* 2020).

The peroxymonosulfate-based AOPs (PMS-AOPs) have gained wide attention due to the asymmetric structure of PMS that is more easily activated to generate ROS. Additionally, the transportation and storage of PMS are more convenient, and there are various ways to activate PMS, such as thermal activation, ultrasound-assisted activation, and ultraviolet radiation (Song *et al.* 2023). As the process of external energy supply involves many uncontrollable factors, its operation is complicated and inconvenient, and the potential for widespread usage is restricted. Transition metals and ions, including Ni, Mn, Fe, Co, Ag, Co2+, Ni2+, Fe3+, Mn2+, V3+, and Fe2+ (Hu *et al.* 2019; Kang *et al.* 2019; An & Xiao 2020), especially Co/Co2, with particular emphasis on Co/Co2+, have the potential to activate PMS and produce highly active substances. The utilization of transition metals has emerged as an alternate option for proficiently eliminating and breaking down contaminants through the activation of PMS.

In recent years, MOF/PMS-AOPs have attracted an increasing amount of interest. Metal-organic frameworks (MOFs) with three-dimensional pore structures (Wang *et al.* 2021c; Xue *et al.* 2022; Zhang *et al.* 2022b; Cao *et al.* 2023) are a kind of

coordination polymers that developed rapidly in the last two decades. The huge specific surface area and regular rhombic dodecahedral crystal shape of Co-based ZIFs (ZIF-67) (commonly used MOF material) are undoubtedly a good choice for catalyst materials (An *et al.* 2018), and numerous carbon-based materials have been utilized as support templates to evenly distribute ZIF metal oxides to improve their stability and reusability (Xu *et al.* 2022). However, the poor stability of ZIF-67, easy overflowing of cobalt, and inconvenient separation from the solution will affect the repetitive applicability of catalysts based on the MOF and cause recontamination. In order to conquer these drawbacks, nowadays, high-temperature treatments have been applied for improvement (Long *et al.* 2022). It is reported that carbon and metal nanoparticles were derived from MOFs with organic linkers by a pyrolysis process. Metal nanoparticles could cause carbon graphitization and be controlled in graphite carbon (Yang *et al.* 2021). The unstable carbon atom causes the orderly transformation from a disorder layer structure to a graphite crystal structure and provides a large number of ion-operative pathways after the pyrolysis process (Yang *et al.* 2021).

Carbon precursors are generally used as catalysts (carbon nanotubes, graphene (oxide), and fullerene); however, the synthetic process is expensive and difficult for scale-usage (Xie *et al.* 2022), and thus the selection of suitable carbon-based carrier materials as support template has become a hot concern. Biomass fibers show the merit of widespread and relatively uncomplicated compositions, which are utilized as raw materials of carbon to acquire biochar fiber with a huge surface area and chemical stability (Ye *et al.* 2020). However, bamboo fiber bundles (BFBs) are obtained by a top-down method that is a simpler and more cost-effective method, and BFBs are acquired without further assembly (Jakob *et al.* 2022; Lamaming *et al.* 2022). In addition, fiber bundles are derived from bamboo with microfibril bundles, hollow parenchymal cell framework structures, and the graphitization of BFB can confine metal ions or metal nanoparticles within the graphite carbon. Additionally, BFB have unique microfibril bundles with hollow parenchymal cell framework structures as favorable embedding areas of active sites for the catalytic degradation of contaminants. Besides, carbon-based catalysts tend to mediate a non-radical pathway of singlet oxygen oxidation ($^1O_2$). Additionally, the metal ions obtained by pyrolysis reduction are magnetic, which are easy to recover and reuse. However, there are few studies (Zhao *et al.* 2019; Wang *et al.* 2021b; Liao *et al.* 2022) on bamboo microfibril bundles as carriers for transition metal directly for the catalytic degradation of TCH.

As is well known, there is a mass of harmful viruses and bacteria in the surrounding water. Harmful bacteria and viruses would multiply in large numbers, bringing enormous damage to the health of human beings, and also deteriorates the water environment. Therefore, antibacterial property plays an important role in water treatment. General biochar itself does not kill microorganisms in large quantities and is not effective for long periods (Zhao *et al.* 2021); however, bamboo charcoal fiber bundles have particular bacteriostatic and Co ion also has bactericidal effects (Dai & He 2019). The Co ion penetrates into the bacterial cell wall and inhibits the enzyme activity, leading to the death of bacteria. The combination of bamboo charcoal fiber bundles and Co doubtlessly can be a novel antibacterial material.

In this study, BFBs were selected as the carbon material substrate for coating of ZIF-67 on bamboo fiber bundles (BFB@ZIF-67) via in-situ growth, and then MOF-derived magnetic Co/CoO nanoparticles with porous polyhedron (BCFB@PCo/CoO) were obtained after pyrolysis of ZIF-67 on BFB. The porous polyhedron structure of the ZIF-67 without agglomeration of nanoparticles was maintained after pyrolysis. Crystalline phase, morphology, pore structure, and composition are characterized. In addition, catalytic degradation of the BCFB@PCo/CoO catalysts, cycling stability, and antibacterial properties of the BCFB@PCo/CoO composite were investigated. The degradation mechanism of TCH in the presence of BCFB@PCo/CoO/PMS was discussed. This work provided a novel BCFB@PCo/CoO composite material to activate PMS to effectively promote the catalytic degradation of TCH for sewage purification. The above-mentioned results are important for novel bamboo fiber-based catalysts and extend the utilization of biomass.

2. EXPERIMENT

2.1. Materials

All the materials, reagents, and chemicals were of analytical reagent (AR) grade and used directly without further purification. In this work, bamboo was chosen from Yibin of Sichuan, China. CH_3COOH, NaOH, MeOH, $NaClO_2$, EtOH, Na_2SO_4, NaCl, NaH_2PO_4, Na_2CO_3, peroxymonosulfate (PMS, $2KHSO_5{\cdot}KHSO_4{\cdot}K_2SO_4$, ≥99.5%, AR), $C_4H_6N_2$ (98%), $Co(NO_3)_2{\cdot}6H_2O$(99%), tert-butyl alcohol (TBA, $C_4H_{10}O$, AR), 1,4-benzoquinone (p-BQ, $C_6H_4O_2$, AR), L-histidine ($C_6H_9N_3O_2$, AR), tetracyclines hydrochloride (TCH), 5,5-dimethyl-1-pyrroline N-oxide (DMPO), 2,2,6,6-tetramethyl-4-piperidine (TEMP), and high-purity nitrogen (N_2, ≥99.99%) were used in the experiment.

2.2. Fabrication of fiber BFB

In brief, BFBs were obtained by removing hemicellulose and lignin from natural bamboo (NB). Bamboo bulks (5 mm×5 mm-×20 mm) were treated with 3.5 wt% NaOH solution at 90 °C for 12 h to remove hemicellulose and then washed with deionized (DI) water and immersed in 1 wt% $NaClO_2$ solution at 85 °C for 12 h to remove lignin. Meanwhile, CH_3COOH was used to adjust the pH value (approximately 4.5) and this process was operated twice. The bamboo bulks were then rinsed in DI water to remove residues. Bamboo bulk templates were obtained by freeze-drying bamboo bulk. Finally, the bamboo bulks were twisted into BFB.

2.3. Synthesis of BCFB@PCo/CoO

1.312 g of (2-MI) and 1.164 g of Co $(NO_3)_2$ $6H_2O$ were placed in methanol and named as solution A and solution B, respectively. Later, solution A was poured into the beaker containing solution B, and the mixture was stirred at 120 rpm for 10 min. The purpose of this step was to facilitate better coordination of Co^{2+} ions with the 2-MI (2-mercaptobenzimidazole) organic ligand. 0.3 g of BFB were then added to the mixture and stirred for 5 min. Finally, ZIF-67 was grown *in-situ* on the BFB after being kept at room temperature for 24 h. Subsequently, BFB@ZIF-67 samples were washed several times in the methanol solution to remove residues. BFB@ZIF-67 was then formed after freeze-drying. Finally, a certain amount of BFB@ZIF-67 was heated under a nitrogen atmosphere at 800 °C and the final product BCFB@PCo/CoO was obtained.

2.4. Characterization

The morphology of BFB, BFB@ZIF-67, and BCFB@PCo/CoO was tested by scanning electron microscopy (SEM). X-ray diffraction (XRD) was utilized to study the crystal structure. The chemical state of BCFB@PCo/CoO was investigated by X-ray photoelectron spectroscopy (XPS). Element distribution was characterized by energy-dispersive spectra (EDS). Special surface area and pore size were determined on a Brunner–Emmet–Teller analyzer (Gemini VII 2390, USA). The chemical structure of BCFB@PCo/CoO was confirmed by Fourier transform infrared spectroscopy (FTIR). The absorbency of TCH was determined using a UV–vis spectrophotometer at 357 nm wavelength. Radicals and non-radicals in the reaction system were detected for the identification of activated species and mechanisms were involved by electron paramagnetic resonance (EPR, BRUKER, EMX-PLUS). The magnetic property of the sample was investigated by a vibrating sample magnetometer (VSM) (LakeShore7404). Analysis of TCH intermediates was carried out by a liquid chromatograph tandem mass spectrometer (Agilent Technologies, 6545 Triple Quad LC-MS).

2.5. Catalytic and antibacterial properties

The catalytic degradation process of BCFB@PCo/CoO for TCH was taken in a beaker. The pH value was regulated with HCl and NaOH. The catalyst was added to the TCH solution and stirred for blending, and then 0.4 g/L of PMS was added. Absorbance before and after degradation was measured at 357 nm by a UV–vis spectrophotometer.

The removal efficiency is calculated by the following formula.

$$D_{(\mathrm{TCH},\%)} = \frac{(C_0 - C_t)}{C_0} \times 100\% \tag{1}$$

Dynamics corresponding to the pseudo-first-order rate is calculated according to the following formula.

$$\ln \frac{C_t}{C_0} = -k_{\mathrm{obs}} t \tag{2}$$

where C_0 and C_t are the initial TCH concentration and the tested one, respectively. k_{obs} refers to the rate constant of pseudo-first-order reaction degradation kinetic (min^{-1}) and t is the deposition time (min).

3. RESULTS AND DISCUSSIONS

3.1. Structures and compositions

The preparation process of the BCFB@PCo/CoO composite is illustrated in Figure 1. Natural bamboo was cut into small bulks (5 mm × 5 mm × 20 mm) along a highly anisotropic structure (the direction of radial growth of bamboo) by utility knife. Alkali treatment and $NaClO_2$/CH_3COOH solution treatment are done to remove hemicellulose and lignin (Cui

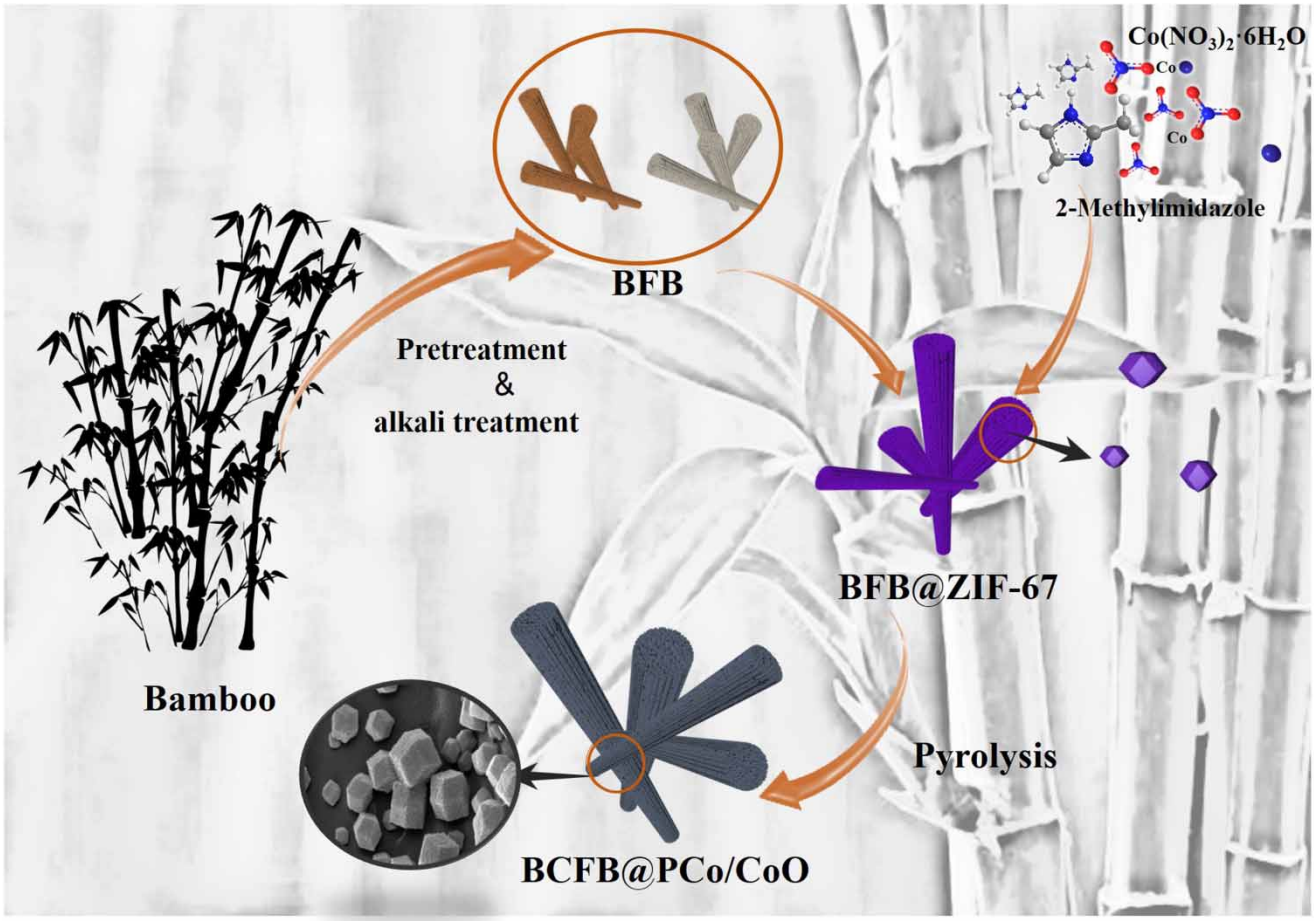

Figure 1 | Schematic diagram of the synthesis of BFB, BFB@ZIF-67, and BCFB@PCo/CoO catalysts.

et al. 2022). The natural yellow color of bamboo (derived from the lignin) gradually disappears and the color of bamboo eventually becomes completely white after chemical delignification (Rasheed *et al.* 2020; Li *et al.* 2022c). First, cobalt nitrate hexahydrate and 2-methylimidazole are mixed into a homogeneous solution. The nucleation rate of ZIF-67 was faster due to the transient high concentration of Co^{2+} and 2-methylimidazole. The color of the solution immediately changed to dark purple when the two solutions were mixed, resulting in the formation of a uniform ZIF-67 solution. Subsequently, the extracted BFB are slowly immersed in the solution, leading to the in-situ uniform growth of ZIF-67 nanocrystal polyhedron on the BFB through the deposition. Finally, the BCFB@PCo/CoO composite is obtained after high-temperature carbonization, which coats the BFB.

Morphologies of BFB, BFB@ZIF-67, and BCFB@PCo/CoO were observed by SEM as shown in Figure 2 and Supplementary material, Figure S1. Natural bamboo stem is composed of rigid microfibril bundles and the neighboring hollow parenchymal cells connect via a matrix of lignin and hemicelluloses. Obviously, bamboo microfibril bundles with hollow parenchymal cell frameworks are obtained after the removal of lignin and hemicellulose as shown in Figures 2(a) and 2(d) and Supplementary material, Figures S1a and S1d. The microfibril bundles and hollow parenchymal cell frameworks are closely connected as support templates for the ZIF-67 nanocrystal. ZIF-67 nanocrystal with a uniform rhombic dodecahedral morphology is densely and uniformly covered on the surface of BFB after ZIF-67 is deposited on BFB (Figure 2(b) and 2(e) and Supplementary material, Figures S1b and S1e). The XRD diffraction patterns (Figure 3(a)) match well with previously published XRD patterns of ZIF-67, confirming the successful loading of ZIF-67. Organic linkers of ZIF-67 turn into carbon frameworks, which is closely connected after the pyrolysis of BFB. Subsequently, Co/CoO nanoparticles are formed and uniformly adhered to the bamboo charcoal fiber bundles and Co/CoO nanoparticles are confined within the graphite carbon.

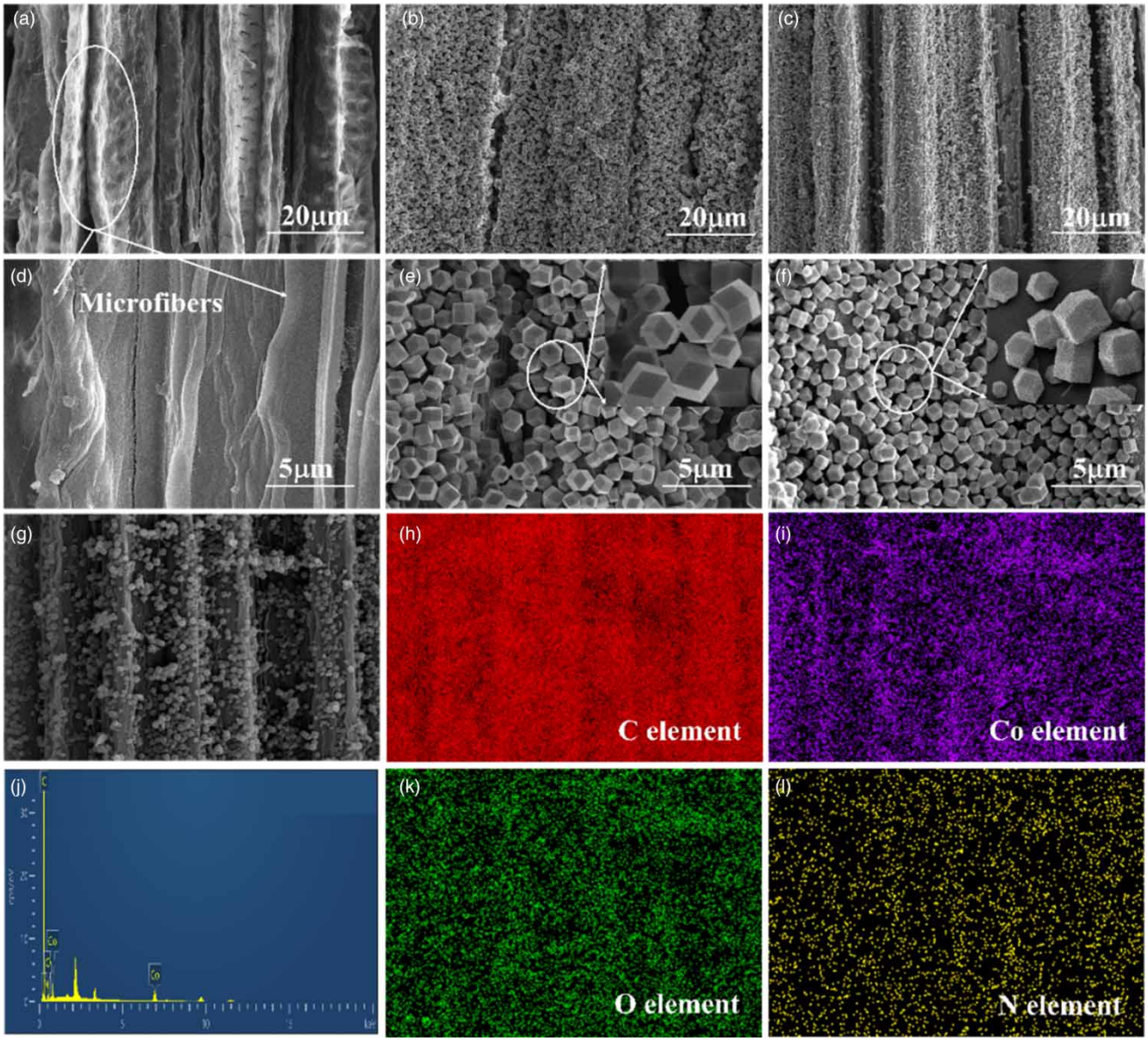

Figure 2 | SEM images of BFB (a, d); BFB@ZIF-67 (b, e); BCFB@PCo/CoO (c, f); and EDS of BCFB@PCo/CoO (g–l).

The nano ZIF-67 is a regular purple rhombic dodecahedron with an average size of 1.27 μm as shown in Supplementary material, Figure S2a. The polyhedron structure of metal nanoparticles is still maintained on the bamboo microfibril bundles with a hollow thin-walled cell framework after high-temperature pyrolysis. Additionally, a large number of pores appear on the surface of the particles as shown in Figures 2(c) and 2(f) and the average size of 0.98 μm is shown in Supplementary material, Figure S2b. The porous characteristic of Co/CoO nanoparticles enhances the specific surface area, which is conductive to active site exposition and pollutant diffusion, therefore, facilitating the catalytic degradation of pollutants. The signals of elements C, O, N, and Co in EDS mapping further confirm the uniform distribution of elements C, O, N, and Co on BCFB@PCo/CoO as shown in Figures 2(g) –2(l).

The crystallinity of BFB, BFB@ZIF-67, and BCFB@PCo/CoO is presented in Figure 3(a). Three obvious crystallization peaks of BFB at $2\theta = 16.0°$, 22.49°, and 35.0° are ascribed to typical cellulose I peaks (Johar *et al.* 2012; Cui *et al.* 2021). Additionally, several new peaks at $2\theta < 26.0°$ appear in the XRD patterns of BFB@ZIF-67, which agree well with (002) and (112) crystal faces of ZIF-67, indicating that ZIF-67 are loaded on BFB successfully (Hou *et al.* 2020). Peak at 26.0°

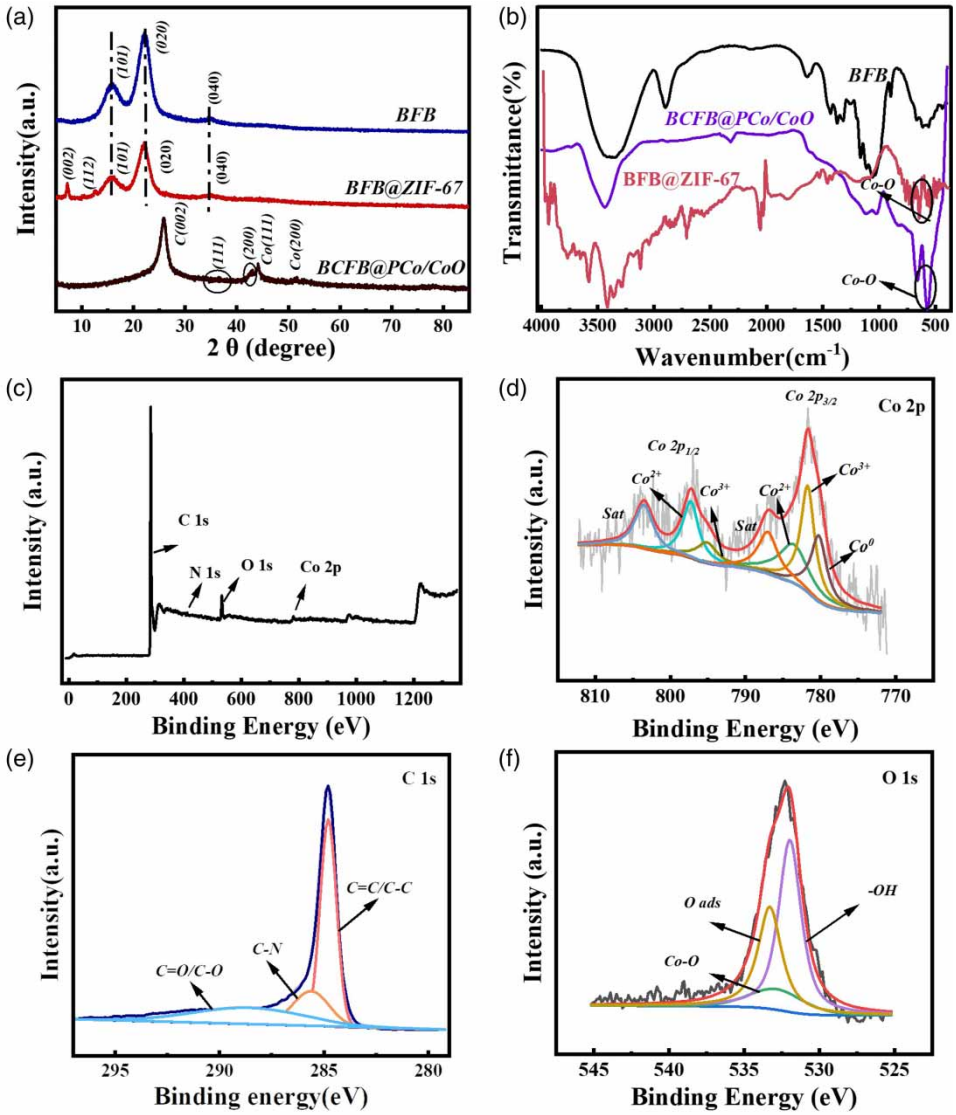

Figure 3 | XRD patterns of BFB, BFB@ZIF-67, and BCFB@PCo/CoO (a), FTIR patternsof BFB, BFB@ZIF-67, and BCFB@PCo/CoO (b), XPS spectra of BCFB@PCo/CoO (c), high-resolution XPS of Co 2p (d), C 1s (e), and O 1s (f).

belongs to the (002) plane of amorphous carbon (Gu *et al.* 2022) in the XRD pattern of BCFB@PCo/CoO, indicating that graphitic carbon is obtained after carbonization. The phenomenon can be explained by the presence of a carbon source and the added Co can be used as a catalyst to generate graphitized carbon. For BCFB@PCo/CoO, the diffraction peak of ZIF-67 disappears and the peak of metallic Co is observed because ZIF-67 decomposes after calcination at high temperature. The diffraction peaks at 44.21° and 51.52° (JCPDS No.15-0806) belong to diffraction peaks at (111) and (200) of metal elemental Co (Hua *et al.* 2022; Wang *et al.* 2022a). Obviously, two peaks at 36.50° and 42.39° correspond to (111) and (200) crystal planes of CoO because Co^{2+} partly turns to Co on the surface of the catalyst after calcination at high temperature due to redox oxidation. In other words, the calcination of ZIF-67 inevitably dislodges its organic skeleton, thus releasing volatile gases such as CO_2 and H_2O, which reduce Co^{2+} to Co, indicating that metallic Co and CoO concurrently exist in BCFB@PCo/CoO (Xu *et al.* 2022). The Co nanoparticles and Co^{2+} ions could combine with the neighboring O atoms to form Co–O bonds and generate more catalytic active sites.

Chemical structures of BFB, BFB@ZIF-67,and BCFB@PCo/CoO are illustrated in Figure 3(b). For BFB, several peaks at 1,670–1,760 cm^{-1} are assigned to the stretching vibration of C = C/C = O. Absorption bands located at approximately

675–870 cm^{-1} are attributed to C–H bending vibration modes. The vibration band of the catalyst at 3,429 cm^{-1} indicates the existence of the –OH, and the absorption bands of BFB@ZIF-67 and BCFB@PCo/CoO are located at approximately 573–667 cm^{-1}, which is attributed to Co–O vibration modes. The result indicates the existence of a Co^{2+} characteristic peak (Liu *et al.* 2020a) after carbonization. Subsequently, BCFB@PCo/CoO shows good catalytic activity of PMS activation for target pollutant degradation.

XPS spectra further confirm the chemical valence of the BCFB@PCo/CoO composite. The spectrum survey XPS (Figure 3(c)) shows that the sharp peaks at 298.12, 545.12, and 781.41 eV can be attributed to the C 1s, O 1s, and Co 2p of the BCFB@PCo/CoO catalyst. Three main peaks of the Co2p spectra at 780.25, 783.61/797.30, 781.73/795.13, and 787.02/803.50 eV are assigned to Co^0($Co\ 2p_{3/2}$), Co^{2+} ($Co\ 2p_{3/2}$ and $Co\ 2p_{1/2}$), Co^{3+} ($Co\ 2p_{3/2}$ and $Co\ 2p_{1/2}$), and satellite peaks (Figure 3(d)), respectively (Li *et al.* 2022a; Xu *et al.* 2022; Zhang *et al.* 2022c). The XPS peak of C 1s is presented in Figure 3(e). Three peaks at 284.79, 285.62, and 288.60 eV can be attributed to C–C/C = C, C–N, and C–O/C = O, respectively (Li *et al.* 2022b; Thanh-Binh *et al.* 2022). C = O sites contribute to $^1O_2$ generation. Three main peaks in the O 1s spectrum at 533.30, 532.83, and 531.96 eV are assigned to absorbing oxygen (O ads), Co–O and –OH of BCFB@PCo/CoO as shown in Figure 3(f), respectively. Co and Co–O (Co^{2+}) hold a rapid reaction rate with PMS due to the unique properties in the process of degradation (Jin *et al.* 2023).

The specific surface area and the distribution of pore size of BCFB@PCo/CoO are important for catalytic performance. Parameters of the BET surface area and the average pore size distribution of BFB, BFB@ZIF-67 and BCFB@PCo/CoO are shown in Table 1. The specific surfaces of the BFB and BFB@ZIF-67 are 3.68 and 66.01 m^2/g, respectively. However, the specific surface of BCFB@PCo/CoO arrives at 302.41 m^2/g, which is greatly higher than those of BFB and BFB@ZIF-67 because the Co nanoparticles and CoO nanoparticles are dispersed on the surface of bamboo charcoal fiber bundles. A larger specific surface area is conducive to the enrichment of active sites, which means that BCFB@PCo/CoO can provide active sites for PMS activation (Zhang *et al.* 2022a). In addition, according to the average pore diameter, the mesopores of BFB could provide a great deal of sites for loading ZIF-67. Additionally, the pores of BFB@ZIF-67 and BCFB@PCo/CoO are mainly composed of mesopores. The mesoporous structure of BCFB@PCo/CoO shows a higher specific surface area and more catalytic active sites; therefore, Co and CoO nanoparticles are generally distributed on the fiber bundles, which is conducive to the catalytic degradation of pollutants.

3.2. Catalytic performance

3.2.1. Catalytic performance of BCFB@PCo/CoO

The catalytic degradation tests are carried out under the conditions of TCH concentration (30 mg/L), PMS dosage (0.4 g/L), catalyst usage (0.2 g/L), and temperature of natural state at 25 °C. The catalytic degradation for TCH of BCFB@PCo/CoO is verified by PMS activation experiments. TCH removal efficiencies of PMS alone, BCFB@PCo/CoO alone, and BCFB@PCo/CoO/PMS in the systems for TCH are shown in Figures 4(a) and 4(b). The low removal rate of PMS alone after the activated PMS degradation reaction indicates that the self-activated oxidation is less effective. However, the BCFB@PCo/CoO/PMS system exhibits the highest degradation efficiency for TCH and the degradation efficiency of BCFB@PCo/CoO without PMS for TCH is 12.99% but the degradation efficiency for TCH is 99.94% with PMS within 15 min. Only a slight removal of TCH is observed for BCFB@PCo/CoO adsorption or PMS oxidation alone. The BCFB@PCo/CoO activates PMS to

Table 1 | Parameters of the BET surface area and average pore size of the BFB, BFB@ZIF-67, BCFB@PCo/CoO, and used BCFB@PCo/CoO catalysts

Catalyst	BET SA [a] (m^2/g)	Micro V [b] (cm^3/g)	Micro A[c] (m^2/g)	Aver. PD [d] (nm)
BFB	3.68	0.00041	0.70	30.36
BFB@ZIF-67	66.01	0.02996	59.13	25.12
BCFB@PCo/CoO	302.41	0.04488	88.88	3.48
Used BCFB@PCo/CoO	205.11	0.01017	21.35	4.45

[a]BET surface area.
[b]Micropore volume.
[c]Micropore area.
[d]Average pore diameter.

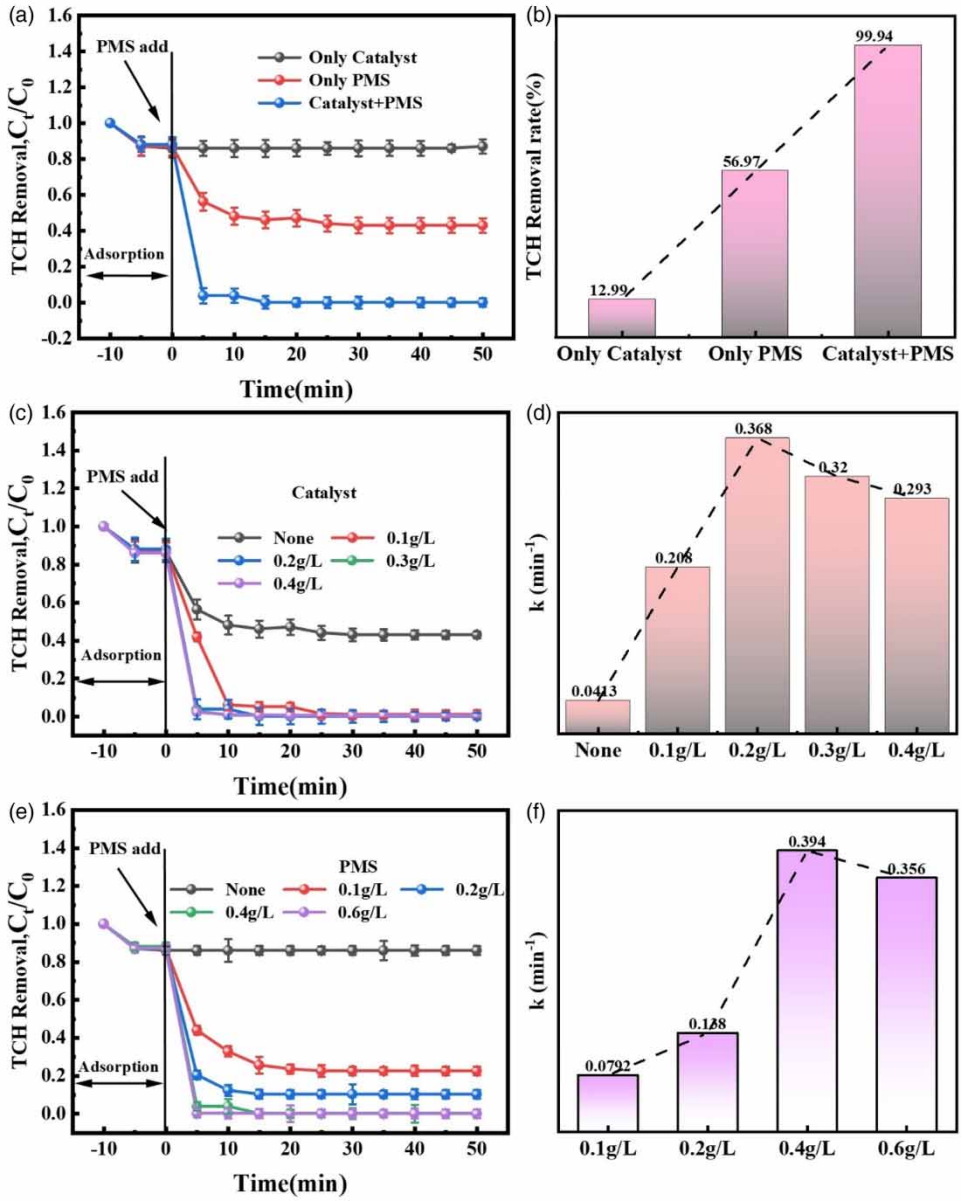

Figure 4 | Effect of different potential factors on the catalytic degradation efficiency of TCH in the BCFB@PCo/CoO/PMS system: degradation efficiency for TCH (a, b); catalyst dosage (c), and the corresponding pseudo-first-order rate of different potential factors on degradation efficiency for TCH (d); PMS dosage (e) and the corresponding pseudo-first-order rate of different potential factors on degradation efficiency for TCH (f). (Optimal conditions: TCH = 30 mg/L, catalyst = 0.2 g/L, PMS = 0.4 g/L, T = 25 °C.)

produce radicals and non-radicals. These results suggest that BCFB@PCo/CoO has the ability to activate PMS to generate large amounts of ROS, thus promoting the catalytic degradation of TCH.

3.2.2. Effects of BCFB@PCo/CoO quality and PMS dose

The effect of BCFB@PCo/CoO dosages on TCH removal is presented in Figure 4(c). It is obvious that the removal efficiency increases significantly with the increase in the BCFB@PCo/CoO catalyst dosage. Only 97% of TCH can be removed after PMS is added by 0.1 g/L of BCFB@PCo/CoO within 15 min, but TCH can be almost completely removed when 0.2 g/L of BCFB@PCo/CoO is used and the removal efficiency reaches 99.94% after PMS is added within 15 min. Additionally, the k_{obs} value increases from 0.04127 to 0.3681 min^{-1} as shown in Figure 4(d). The result can be interpreted

as that the catalyst provides a mass of surface active sites in the whole system with the increase in BCFB@PCo/CoO as the reaction proceeds. In addition, removal efficiency increases with the increase in the amount of the BCFB@PCo/CoO dosage because a mass of radicals and non-radicals are produced by activating PMS, which leads to the increase in the TCH removal efficiency. However, the catalytic degradation performance slightly decreases by overproducing oxidizing radicals caused by the excessive addition of the BCFB@PCo/CoO catalyst, which promotes interaction among the radicals (Equations (4)–(6)). 0.2 g/L of BCFB@PCo/CoO catalyst achieves the desired catalytic degradation; therefore, 0.2 g/L BCFB@PCo/CoO is used in the subsequent test.

PMS is the source to produce radicals and non-radicals in advanced oxidation reactions in the degradation process. The PMS dosage has a remarkable effect on the catalytic degradation of TCH as shown in Figure 4(e). TCH removal efficiency of the BCFB@PCo/CoO/PMS composite shows an accelerated trend with the increase in the PMS dosage. Briefly, TCH removal efficiency increases dramatically from 51.6 to 86.6% when the PMS dosage increases from none to 0.4 g/L, and k_{obs} increases gradually from 0.0792 to 0.394 min^{-1} as shown in Figure 4(f). This phenomenon of improving the removal speed and efficiency of TCH can be explained by the production of more reactive radicals and non-radicals by larger concentrations of PMS in the reaction system. However, the removal efficiency decreases slightly ($k_{obs} = 0.356\ min^{-1}$) when the PMS dosage is increased from 0.4 to 0.6 g/L. On the one hand, a certain amount of PMS is activated by a limited number of active sites on the BCFB@PCo/CoO surface to generate reactive radicals and non-radical promoting the catalytic degradation of TCH. However, it is difficult for the limited BCFB@PCo/CoO dosage to provide adequate activation sites when the concentration of PMS is high. On the other hand, in order to achieve the purpose of holding the catalytic degradation reaction at a suitable level, $SO_4^{\cdot-}$ and $^{\cdot}OH$ radicals could produce a mutual effect and self-extinguishing reactions (Equations (3)–(5)) (Liu *et al.* 2021).

$$SO_4^{\cdot-} + {}^{\cdot}OH \rightarrow HSO_5^- \quad (3)$$

$$^{\cdot}OH + {}^{\cdot}OH \rightarrow H_2O_2 \quad (4)$$

$$SO_4^{\cdot-} + SO_4^{\cdot-} \rightarrow S_2O_8^{2-} \quad (5)$$

3.2.3. Effects of initial TCH concentration, pH value, and temperature

The influence of initial TCH concentration on catalytic degradation efficiency was tested and the results are presented in Figure 5(a). Catalytic degradation efficiency shows a downward trend with the increase in the initial concentration of TCH. TCH is completely degraded with the initial concentration of 30 mg/L of TCH within 30 min. However, the catalytic degradation efficiency decreases obviously with the increase in the initial concentration of TCH from 40 to 100 mg/L and the k_{obs} value decreases from 0.255 to 0.0603 min^{-1}. The phenomenon can be explained by that the radicals and non-radicals are generated relatively stable because of the unchangeable amount of PMS and catalyst in the system.

It has been reported that pH is one of the crucial factors for the degradation efficiency of antibiotic pollutants (Yao *et al.* 2023). Various types of TCH can be detected in environments with different pH values. Therefore, it is necessary to study the effect of the BCFB@PCo/CoO/PMS system on TCH catalytic degradation efficiency at different initial pH values (1.0–9.0) as shown in Figure 5(b). Good efficiency can be achieved under acidic and alkaline environments. The degradation efficiency of TCH decreases to 90.20% and k_{obs} is 0.139 min^{-1} when the initial pH is 9.0, which suggests that higher pH reaction conditions negatively affect activating PMS. PMS is dissolved in alkaline without adequate oxidizing groups $^1O_2$ and $\cdot O_2^-$ (Liu *et al.* 2017) produced. The efficiency is only 79.42% at pH = 1.0 under acidic conditions and k_{obs} is 0.0794 min^{-1}. The reaction between H^+ stabilization and peroxide bond (–O–O–) leads to the hindered degradation rate of TCH due to interfacial repulsion (Wang *et al.* 2016; Fu *et al.* 2019; Liu *et al.* 2020b) (Equations (6) and (7)).

$$HSO_5^- + OH^- \rightarrow H_2O + SO_5^{2-} \quad (6)$$

$$HSO_5^- \rightarrow H^+ + SO_5^{2-} \quad (7)$$

The effect of temperature on TCH degradation is shown in Figure 5(c). Obviously, the degradation efficiency of TCH increases under the catalytic action of the catalyst with the change of temperature from 5 to 25 °C and slightly decreases from 25 to 45 °C. These results indicate that the temperature plays an important role in PMS activation to catalyze organic

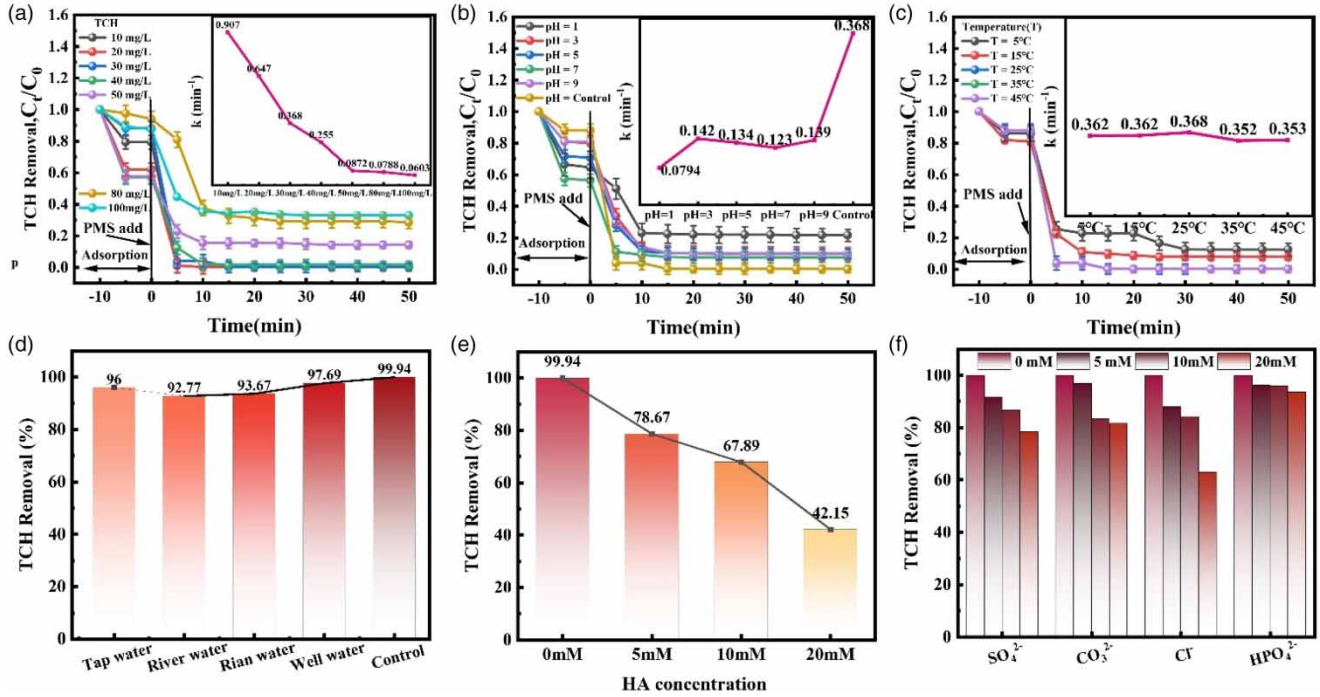

Figure 5 | Effect of different potential factors on the catalytic degradation efficiency of TCH in the BCFB@PCo/CoO/PMS system: TCH concentration (a); pH value (b); temperature (c) and the corresponding pseudo-first-order rate of different potential factors on the degradation efficiency for TCH added. Practical water body on TCH degradation (d); humic acid (e); and different concentration of Cl^-; SO_4^{2-}; $H_2PO_4^-$; CO_3^{2-} (f). (Optimal conditions: TCH = 30 mg/L, Catalyst = 0.2 g/L, PMS = 0.4 g/L, T = 25 °C.)

pollutants. The possible reason may be attributed to the high temperature. PMS can quickly contact the catalyst surface to promote electron transfer in radical products, and pollutant molecules are simultaneously affected to move faster at high temperatures (Li *et al.* 2023b). However, the catalytic degradation performance slightly decreases by overproducing oxidizing radicals caused by higher temperatures, which promotes interaction among the radicals.

3.2.4. Effect of practical water body, humic acid, and inorganic anions

The degradation efficiency of BCFB@PCo/CoO/PMS for real water was also investigated to evaluate the potential of BCFB@PCo/CoO. Tap water, river water, rainwater, and well water were used as the solvents of the TCH solution to investigate the influent of different water quality on TCH degradation as shown in Figure 5(d). The BCFB@PCo/CoO/PMS system still could maintain a high removal capacity toward TCH in tap water, river water, rainwater, and well water with degradation degrees of 96, 91.8, 93.7, and 92.5%, respectively. It is found that the degradation efficiency for TCH in river water decreases distinctly, which might be related to the presence of high-concentration ions and reducing matters in the river water. The results further imply that BCFB@PCo/CoO/PMS possesses the general applicability for practical water treatment.

Natural organic matter (NOM) almost exists in wastewater everywhere (Jin *et al.* 2023). As an example, humic acid (HA) is chosen to study how NOM affects AOPs. The competing degradation of HA and TCH with the produced radicals and non-radicals may be the reason for the decrease in TCH degradation efficiency from 99.94 to 42.15% when the concentration of HA is 20 mM as shown in Figure 5(e). The presence of HA would dramatically increase the consumption of the generated ROS, inhibiting the breakdown of the TCH contaminants.

A large number of NOM, inorganic matter, and common anions are generally presented in the water system in the natural state of the environment. Co-existing organic and inorganic anions affect the removal efficiency of BCFB@PCo/CoO for TCH. On the one hand, existing organic and inorganic anions may react with PMS to prevent the generation of radicals and non-radicals; on the other hand, co-existing organic and inorganic anions may interact with free radicals and non-radicals. The degradation efficiency for TCH in different concentrations of co-existing anions is shown in Figure 5(f). The degradation

efficiency for TCH is partly inhibited as the concentration of ions increases. In 20 mM of Cl^-, SO_4^{2-}, CO_3^{2-}, and $H_2PO_4^{2-}$, the efficiency achieves 62.88, 78.46, 81.57, and 93.67%, respectively. Particularly, Cl^- ions show significant inhibition for TCH degradation with the removal efficiency of only 62.88% within 60 min due to the scavenging effect of Cl^-. The active radicals can be changed by Cl^- to form $^{\cdot}Cl$ radicals in lower redox potential (Han & Xiao 2022). Furthermore, it was observed that $H_2PO_4^{\cdot}$ as well as with a low potential played a significant role in this process due to the quenching effect of $H_2PO_4^-$ on $^{\cdot}OH$ and $SO_4^{\cdot -}$ radicals (Luo *et al.* 2020). The inhibitory effect of ions may be related to the following reactions (Equations (8)–(17)) (Pang *et al.* 2022).

$$Cl^- + SO_4^{-\cdot} \rightarrow SO_4^{2-} + Cl^{\cdot} \quad (8)$$

$$Cl^- + {}^{\cdot}OH \rightarrow {}^{\cdot}Cl + OH^- \quad (9)$$

$$2Cl^- + HSO_5^- + H^+ \rightarrow SO_4^{2-} + Cl_2 + H_2O \quad (10)$$

$${}^{\cdot}Cl + {}^{\cdot}Cl \rightarrow Cl_2 \quad (11)$$

$$Cl^- + {}^{\cdot}Cl \rightarrow {}^{\cdot}Cl_2^- \quad (12)$$

$$CO_3^{2-} + SO_4^{-\cdot} \rightarrow SO_4^{2-} + CO_3^{-\cdot} \quad (13)$$

$$CO_3^{2-} + {}^{\cdot}OH \rightarrow OH^- + CO_3^{-\cdot} \quad (14)$$

$$H_2PO_4^- + SO_4^{-\cdot} \rightarrow SO_4^{2-} + H_2PO_4^{\cdot} \quad (15)$$

$$H_2PO_4^- + {}^{\cdot}OH \rightarrow OH^- + H_2PO_4^{\cdot} \quad (16)$$

$$SO_4^{2-} + {}^{\cdot}OH \rightarrow SO_4^{-\cdot} + OH^- \quad (17)$$

3.3. Identification of major ROS

The catalytic degradation properties of TCH by BCFB@PCo/CoO/PMS is mainly related to both radical and non-radical pathways (Ghauch *et al.* 2017). A series of classical scavengers such as MeOH, p-BQ, TBA, and L-His was used to reveal ROS during TCH degradation. Among them, MeOH, p-BQ, TBA, and L-His (Zhong *et al.* 2020) were utilized for quenchers of $^{\cdot}SO_4^-$, $^{\cdot}O_2^-$, $^{\cdot}OH$, and $^1O_2$, respectively (Luo *et al.* 2021; Qi *et al.* 2021; Xiong *et al.* 2023). As shown in Figures 6(a) and 6(b), a significantly restrained effect with adding quenching agents P-BQ, TBA, and L-histidine and the TCH removal efficiencies just are 52.87, 43.67, and 58.00% within 60 min and k_{obs} values are 0.02699, 0.02746, and 0.03597 min^{-1}, respectively. The removal efficiency for TCH is only 6.19% after the introduction of MeOH, and k_{obs} is 0.13995 min^{-1}. The results indicate that $^{\cdot}OH$, $^{\cdot}O_2^-$, and $^1O_2$ play an important role via BCFB@PCo/CoO/PMS system in TCH catalytic degradation. Overall, the catalytic degradation of TCH in wastewater mainly results from the synergistic effects of radicals and non-radicals.

To confirm the presence of an active substance in the BCFB@PCo/CoO/PMS catalyst system, the EPR was measured. As shown in Figures 6(c)–6(d), 5,5-dimethyl-1-pyrroline N-oxide (DMPO) and 2,2,6,6-tetramethy-l-4-piperidinol (TEMP) were used as raw materials to capture the active substances of the catalytic system generally. DMPO was utilized to capture $\cdot SO_4^-$, $\cdot OH$, and $^{\cdot}O_2^{-\cdot}$. TEMP was used to capture $^1O_2$. The clear signals of 1:2:2:1 DMPO-$^{\cdot}OH$ and 1:1:1:1:1:1 DMPO-$^{\cdot}SO_4^-$ prove that the presence of $SO_4^{-\cdot}$ and $^{\cdot}OH$ is generated at the same time in the BCFB@PCo/CoO /PMS catalyst system. The result agrees with the quenching tests as shown in Figure 7(a); in addition, the peak intensity of $\cdot OH$ is significantly higher than that of $^{\cdot}SO_4^-$. Similarly, the obvious signals of 1:1:1 TEMP-$^1O_2$ and 1:1:1:1 DMPO-$^{\cdot}O_2^-$ characteristic peaks can also be found in the catalyst degradation system, which indicates that $O_2^{-\cdot}$ and $^1O_2$ are also involved in TCH degradation. The main activation process of the catalytic degradation of TCH can be expressed as shown in Equations (21)–(25). Transition metal Co(0) reacts first with PMS, leading to the oxidation of Co(0) to Co(2+) and subsequently to Co(3+) (Liu *et al.* 2019). PMS acts as both an oxidant and a reductant, facilitating the cycle of Co (2+)/Co (3+) transformation. Transition activates in large quantities, generating numerous radicals and non-radical species, which then attack complex molecules of TCH and intermediates, achieving effective pollutant degradation. The possible activation mechanism of PMS

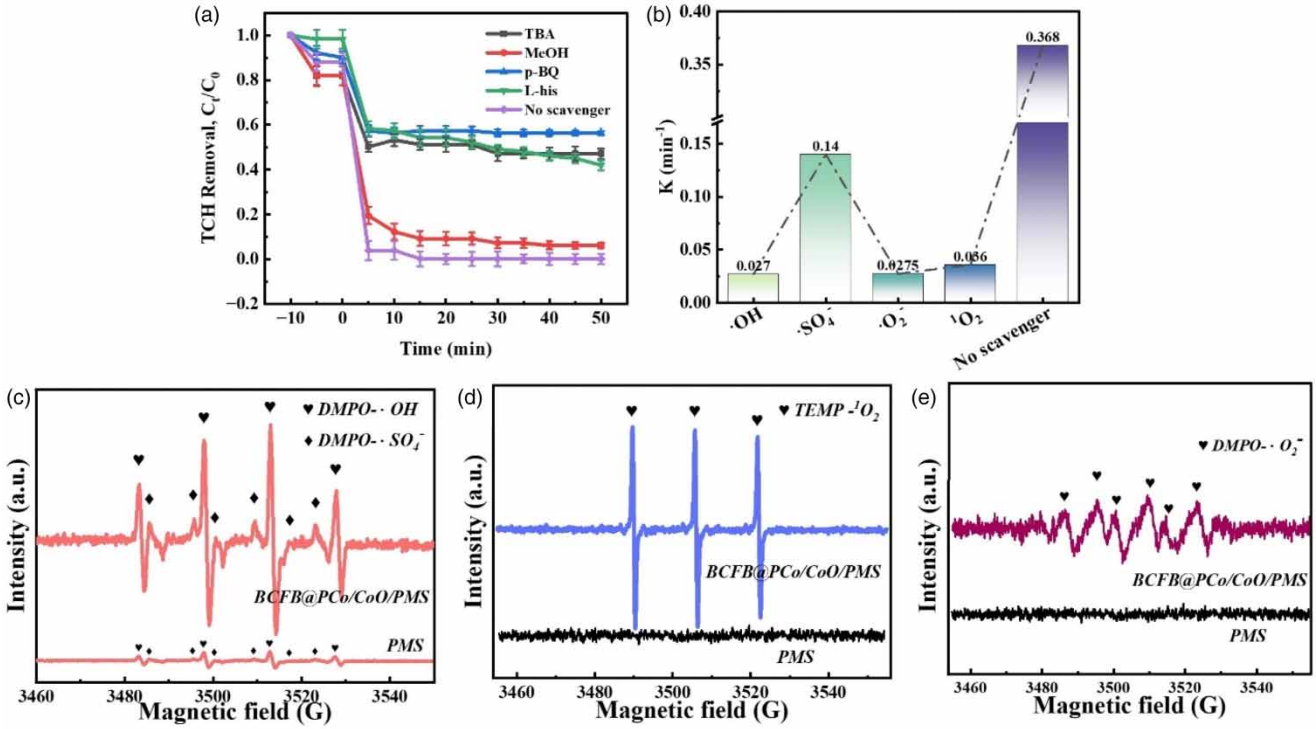

Figure 6 | The quenching experiment (a) and the corresponding pseudo-first-order rate (b). EPR spectra (c, d, and e) of the BCFB@PCo/CoO/PMS system. (Experimental conditions: TCH = 30 mg/L, Catalyst = 0.2 g/L, PMS = 0.4 g/L, T = 25 °C, DMPO = 100 mM, TEMP = 100 mM.)

by BCFB@PCo/CoO is illustrated in Figure 7, demonstrating the significant role of PMS in the degradation process (Liu *et al.* 2019).

$$Co^0 + 2HSO_5^- \rightarrow Co^{2+} + 2SO_4^{\cdot -} + 2^{\cdot}OH \quad (18)$$

$$Co^{2+} + HSO_5^- \rightarrow Co^{3+} + SO_4^{\cdot -} + OH^- \quad (19)$$

$$Co^{3+} + HSO_5^- \rightarrow Co^{2+} + SO_5^{\cdot -} + H^+ \quad (20)$$

$$Co^0 + 2Co^{3+} \rightarrow 3Co^{2+} \quad (21)$$

$$HSO_5^- + SO_5^{2-} \rightarrow {}^1O_2 + SO_4^{2-} + HSO_4^- \quad (22)$$

$$SO_5^{\cdot -} + SO_5^{\cdot -} \rightarrow {}^1O_2 + 2SO_4^{2-} \quad (23)$$

$$SO_5^{2-} + H_2O \rightarrow O_2^{\cdot -} + SO_4^{\cdot -} + H^+ \quad (24)$$

$$TCH + ROS\ (O_2^{\cdot -}/SO_4^{\cdot -}/{}^{\cdot}OH/{}^1O_2) \rightarrow Intermediates \rightarrow CO_2 + H_2O \quad (25)$$

3.4. TCH degradation pathway

The active substances ($SO_4^{\cdot -}$, ·OH, $O_2^{\cdot -}$, $^1O_2$) produced by the BCFB@PCo/CoO/PMS system can inspire the catalytic degradation of TCH macromolecules and generate low-molecular-weight products. HPLC-MS measurement in a positive ion mode was used to analyze catalytic degradation intermediates of the BCFB@PCo/CoO/PMS for TCH and shows the catalytic degradation intermediates and their possible molecule structures. The majority of catalytic degradation intermediates were detected when the test time was prolonged (the TCH intermediates and their possible molecule structures are shown in Supplementary material, Figure S3 and Table S1). The three possible degradation pathways are illustrated in Figure 8. For pathway I, P1(m/z = 417.26) is produced by N-demethylation under the combined attacks of the $SO_4^{\cdot -}$, $^1O_2$ and ·OH (Hu *et al.* 2021). After that, P1 is further broken down into P2 (m/z = 338.34) and P3 (m/z = 222.18) through a range of ring-opening and dealkylation reactions. Subsequently, P4 (m/z = 318.24) is produced through dealcoholization and

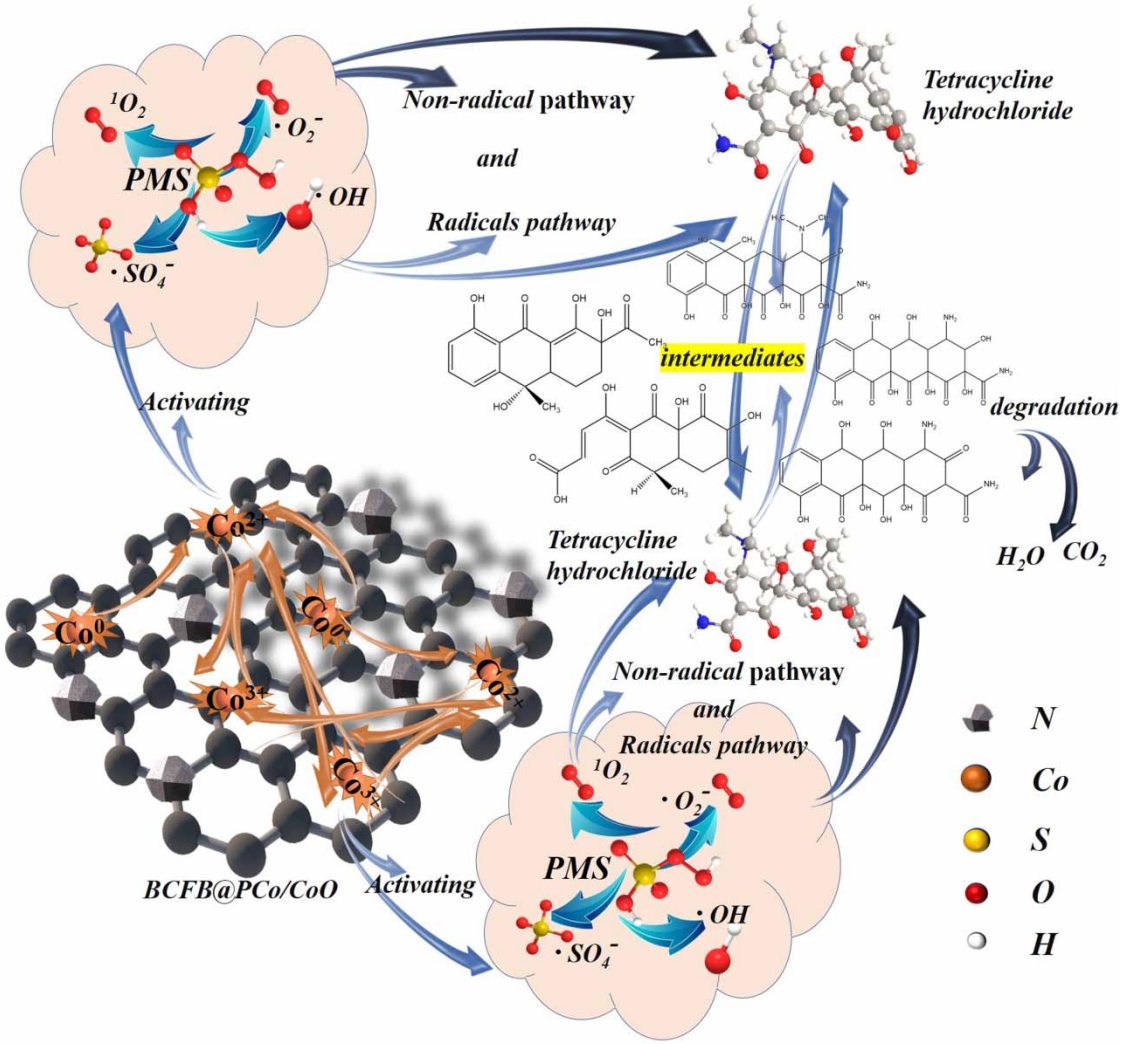

Figure 7 | The possible activation mechanism of PMS by BCFB@PCo/CoO.

ring-opening and P4 is further oxidized to P5 ($m/z = 141.11$). For pathway II, the double bond of TCH through the addition process, then by hydroxyl rearrangement transformed into P6 ($m/z = 461.16$). However, the double bond of P6 is attacked by ·OH and P7 ($m/z = 477.15$) consists of the –OH addition to the double bond (Han *et al.* 2022a). Ultimately, the aromatic ring of P7 is attacked by –OH to form P8 ($m/z = 495.16$). In pathway III, TCH is attacked by $^1O_2$ and converted to P9 ($m/z = 491.30$) by oxygen oxidation. P10 ($m/z = 477.15$) is generated by demethylation of P9. On the one hand, the active substance is produced from PMS activation and attacked P10 to acquire P11 ($m/z = 451.16$) (Zhong *et al.* 2020). The generations of P12 ($m/z = 212.84$) resulted from the decarbonylation (Wang *et al.* 2021a), ring-opening, and dehydration of P11 (Wang *et al.* 2021a). On the other hand, P13 ($m/z = 453.22$) is produced by further demethylation and decarbonylation (Zhu *et al.* 2022). Further deamidation and dihydroxylation occur on P13-produced P14 ($m/z = 343.07$). Subsequently, all the intermediates are continued oxidized to smaller molecules, such as P15, P16, and P17. The catalytic degradation intermediates are generated via acylation, ring-opening, deamination, dihydroxylation, acidification diacylation, and dehydration. All the intermediates are eventually effectively catalyzed by the catalyst to environmental-friendly H_2O and CO_2, which greatly reduces ecotoxicity.

3.5. Catalyst reusability and stability

Considering the production cost, the reusability as a useful basis was evaluated for the comprehensive usage effect of the catalyst system in practical applications. In order to further verify the catalytic stability of the BCFB@PCo/CoO/PMS catalyst, a

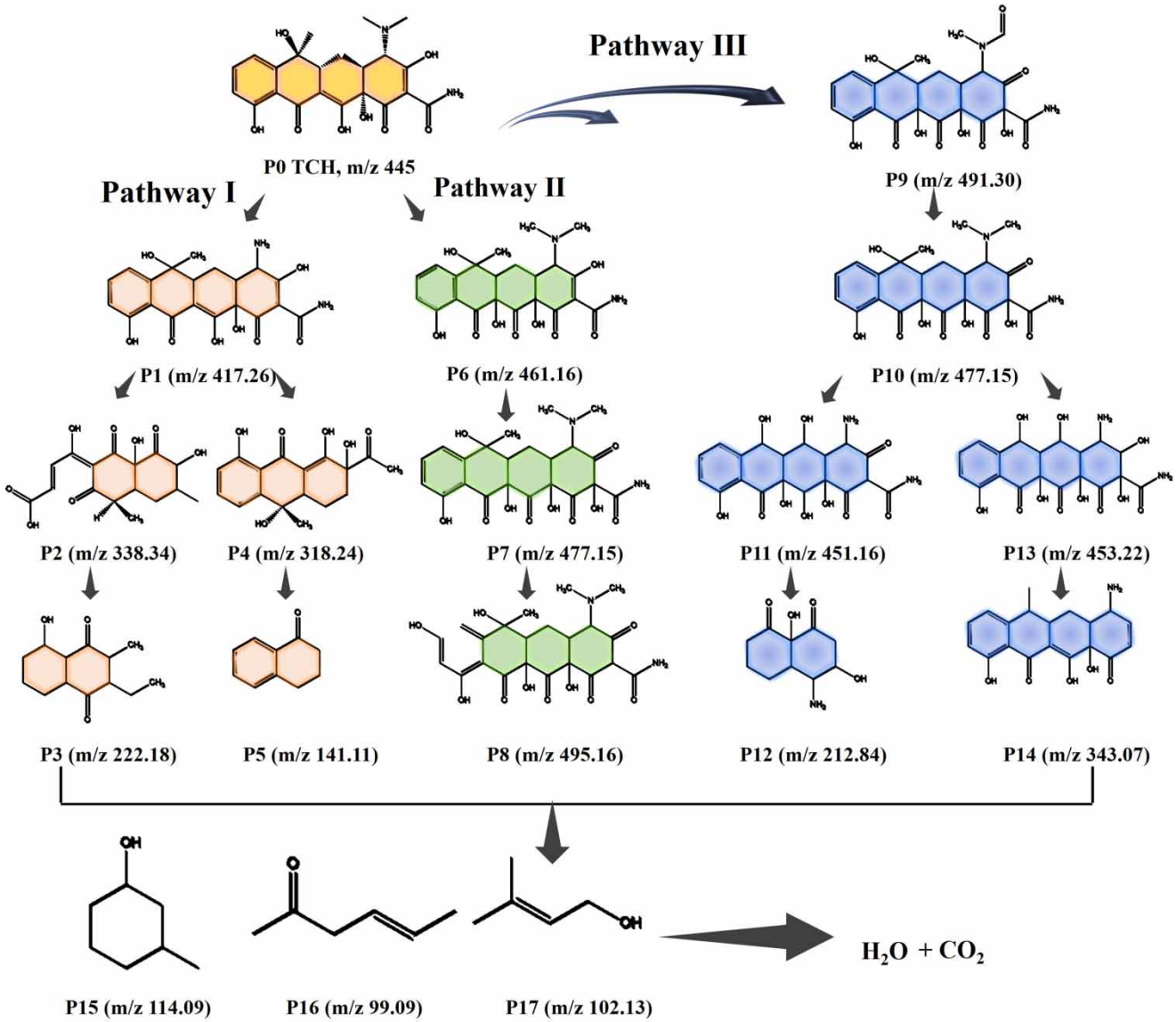

Figure 8 | Possible degradation pathways of TCH in BCFB@PCo/CoO/PMS.

recyclability test was carried out under suitable conditions. The specific surface area of the composite decreases from 302.41 to 205.11 m^2/g after the reaction is shown in Table 1, SEM images (Supplementary material, Figures S1g–S1i), and results of XPS and XRD after the reaction are shown in Figures 9(a)–9(e). In the XRD of BCFB@PCo/CoO and XPS spectrum of Co 2p after the reaction, the interconversion process of transition metal Co, Co^{2+}, and Co^{3+} leads to changes in content, which further indicates that Co nanoparticles and CoO nanoparticles are loaded well after reuse and the catalyst shows strong structural stability. The pursuit of production benefits is confirmed; thus, the result elucidates that the coexistence of Co and oxidation states with carbon skeleton is beneficial to promote the efficiency of the oxygen transfer process. Additionally, only a part of TCH molecules is adsorbed on the catalyst surface, just little blocking a small part of the pore and occupying a small part of the active site. A small amount of Co substance was removed from BCFB@PCo/CoO/PMS after washing. The catalytic performance of BCFB@PCo/CoO is better than that of the latest research performance of Co-based material as shown in Table 2, indicating that the BCFB@PCo/CoO composite can become a good alternative novel catalyst.

In addition, the TCH removal rate in the BCFB@PCo/CoO/PMS system was still higher than 78% after five recycles, as shown in Supplementary material, Figure S4a. The results demonstrate that the BCFB@PCo/CoO/PMS system has an

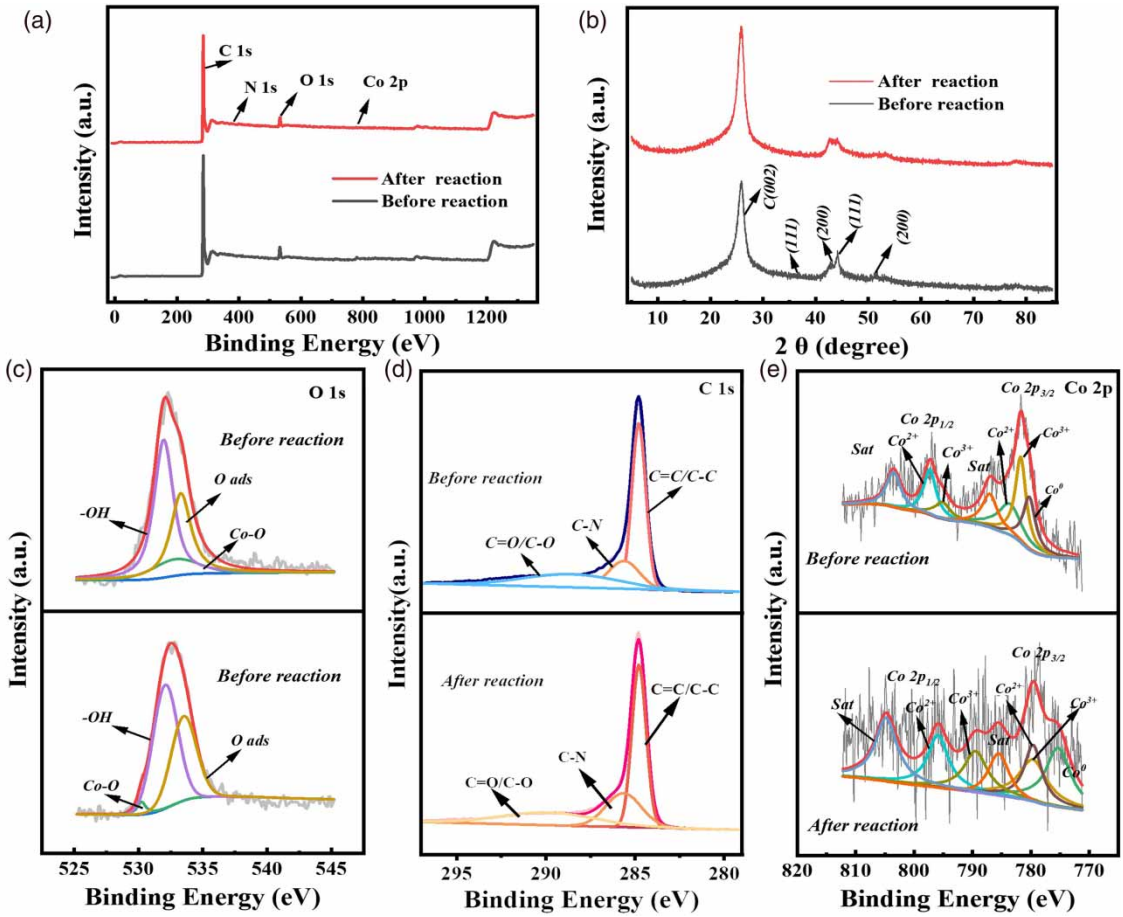

Figure 9 | XPS pattern of before/after degradation reaction (a), XRD pattern of before/after degradation reaction (b), high-resolution XPS spectra of O1s (c), C1s (d), and Co 2p (e), for BCFB@PCo/CoO.

Table 2 | The catalytic performance of TCH in latest research works on Co-based materials

Catalysts	Catalysts dosage (g/L)	Initial concentration of TCH (mg/L)	PMS dosage (mM)	Removal time (min)	Removal efficiency for TCH (%)	Reference
Co@NCNTs-600	0.12	20	2	20	93.10	Hu *et al.* (2022)
Co-N/KC-900	0.16	20	1	15	99	Zhu *et al.* (2022)
FeCo10	0.3	22.5	0.5	10	95.1	Han *et al.* (2022b)
CoFe0.8@NCNT@CA	0.4	40	2	20	97.1	Wu *et al.* (2022)
Co_2SnO_4-SnO_2	1	50	1.5	20	94.9	Wang *et al.* (2022b)
Fe-Co-N@HCCs	0.2	30	2	40	92.6	Guan *et al.* (2022)
CZA-1000/PMS	0.04	20	1	30	99.8	Hua *et al.* (2022)
BCFB@PCo/CoO	0.2	30	2	15	99.94	This work

excellent reusability and can become a good alternative novel product. The magnetic characterization of the BCFB@PCo/CoO composite was determined using VSM at room temperature as shown in Supplementary material, Figure S4b. The saturation magnetization strength (Ms) of BCFB@PCo/CoO is 4.09 emu/g, which allows for fast and easy separation of BCFB@PCo/CoO from aqueous solutions under an applied magnetic field. Supplementary material, Figure S3b shows that BCFB@PCo/CoO can be attracted by the magnet, and thus, the BCFB@PCo/CoO composite shows good potential in removing pollutants from aqueous solutions due to the property of easy separation.

3.6. Antibacterial properties

Antimicrobial properties of the BCFB@PCo/CoO composite against *Escherichia coli* (*E. coli*) and *Gram-positive Staphylococcus aureus* (*S. aureus*) were carried out according to AATCC 147. The obvious 11 and 12 mm of bacteriostatic zone indicate that BCFB@PCo/CoO has excellent antibacterial activity against *E. coli* and *S. aureus* as shown in Figure 10, respectively. Bamboo charcoal fiber bundles have particularly bacteriostatic effects and Co ion themselves also have bactericidal effects. The Co ions penetrated into the bacterial cell wall and inhibited the enzyme activity, killing the bacteria (Li *et al.* 2023a). The synergistic action of bamboo charcoal fiber bundles and Co ion make BCFB@PCo/CoO to have an obvious bacteriostatic effect, preventing bacteria from growing on BCFB@PCo/CoO, to facilitate catalytic degradation process, and the purpose of purification sewage is quickly achieved.

4. CONCLUSION

A composite of MOF-derived magnetic Co/CoO nanoparticles with porous polyhedron was successfully embedded in bamboo charcoal microfibril bundles (BCFB@PCo/CoO) with hollow parenchymal cell frameworks derived from bamboo charcoal fiber bundles. The result shows that the specific surface area of the obtained BCFB@PCo/CoO is 302.41 m^2/g. The degradation efficiency of BCFB@PCo/CoO/PMS for TCH could reach 99.94% within 15 min. Additionally, BCFB@PCo/CoO/PMS is less affected by environmental temperature, co-existing anions (except Cl^-), humic acid in water, and different practical natural water, and shows a high efficiency in a broad pH range of 1.0–9.0. Results of quenching and EPR technology demonstrate that $SO_4^{\cdot-}$, ·OH, $O_2^{\cdot-}$, and $^1O_2$ are involved in PMS activation and both radical and non-radical pathways presented a superior performance of the BCFB@PCo/CoO/PMS system in TCH degradation. Co and CoO nanoparticles were still well loaded on bamboo charcoal fiber bundles after the catalytic reaction. The possible degradation pathways were explored by liquid chromatography–mass spectrometry (LC–MS) analysis including the cycles of Co^0 →

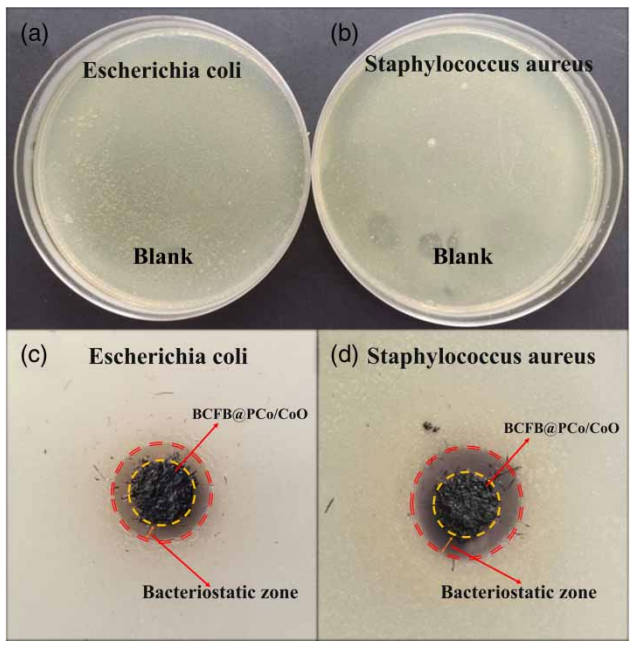

Figure 10 | The antibacterial effect of the blank and BCFB@PCo/CoO for *Escherichia coli* (a, c) and *Staphlococcus aureus* (b, d).

$Co^{2+} \rightleftharpoons Co^{3+}$. The high degradation efficiency was maintained well after five recycles. The proposed BCFB@PCo/CoO composite demonstrates high degradation efficiency toward TCH, good regeneration capability, good antibacterial properties, and low secondary contamination toward the environment and it could be effectively recycled and reused by magnetic separation. Based on the intermediates measured by HPLC-MS, three degradation pathways of TCH were proposed. Therefore, the BCFB@PCo/CoO will be a potential catalyst for the purpose of purification of tetracycline-containing domestic/industrial/medical wastewater.

AUTHORS CONTRIBUTIONS

All authors contributed to the study's conception and design. Material preparation, data collection, and analysis were performed by L.D., C.C., M.Y., and S.J. The first draft of the manuscript was written by L.D. The investigation and methodology by J.L. The conceptualization, project administration, funding acquisition, supervision, writing review, and editing by R.G. All authors commented on previous versions of the manuscript and all authors read and approved the final manuscript.

FUNDING

This work was supported by the Science and Technology Planning Project of Sichuan Province (No. 2020YFN0150), Cooperation Project between Sichuan University and Yibin City (2020CDYB-5), the Opening Project of Jiangsu Engineering Research Center of Textile Dyeing and Printing for Energy Conservation, Discharge Reduction and Cleaner Production (ERC) (SDGC2223), and Yibin unveiling and commanding project (00308055A1282).

DATA AVAILABILITY STATEMENT

All relevant data are included in the paper or its Supplementary Information.

CONFLICT OF INTEREST

The authors declare there is no conflict.

REFERENCES

An, L. & Xiao, P. 2020 Zero-valent iron/activated carbon microelectrolysis to activate peroxydisulfate for efficient degradation of chlortetracycline in aqueous solution. *Rsc Advances* **10** (33), 19401–9.

An, S., Zhang, G., Wang, T., Zhan, W., Li, K., Song, C., Miller, J. T., Miao, S., Wang, J. & Guo, X. 2018 High-density ultra-small clusters and single-atom Fe sites embedded in graphitic carbon nitride (g-C3N4) for highly efficient catalytic advanced oxidation processes. *Acs Nano* **12** (9), 9441–9450.

Cai, T., Teng, Z., Wen, Y., Zhang, H., Wang, S., Fu, X., Song, L., Li, M., Lv, J. & Zeng, Q. 2022 Single-atom site catalysts for environmental remediation: recent advances. *Journal of Hazardous materials* **440**, 129772.

Cao, Y., Yue, L., Li, Z., Han, Y., Lian, J., Qin, H. & He, S. 2023 Construction of Sn-Bi-MOF/Ti3C2 Schottky junction for photocatalysis of tetracycline: performance and degradation mechanism. *Applications of Surface Science* **609**, 155191.

Cui, F., Li, H., Chen, C., Wang, Z., Liu, X., Jiang, G., Cheng, T., Bai, R. & Song, L. 2021 Cattail fibers as source of cellulose to prepare a novel type of composite aerogel adsorbent for the removal of enrofloxacin in wastewater. *International Journal of Biological Macromolecules* **191**, 171–181.

Cui, C., Yang, M., Zhai, J., Bai, W., Dai, L., Liu, L., Jiang, S., Wang, W., Ren, E., Cheng, C. & Guo, R. 2022 Bamboo cellulose-derived activated carbon aerogel with controllable mesoporous structure as an effective adsorbent for tetracycline hydrochloride. *Environmental Science and Pollution Research* **30**, 12558–12570.

Daghrir, R. & Drogui, P. 2013 Tetracycline antibiotics in the environment: a review. *Environmental Chemistry Letters* **11** (3), 209–227.

Dai, S. & He, Y. 2019 Synergistic antibacterial effect of Zn, Co doped and Co/Zn co-doped titania nano-materials. *Journal of Functional Materials* **50** (10), 10133–9.

Duan, P., Qi, Y., Feng, S., Peng, X., Wang, W., Yue, Y., Shang, Y., Li, Y., Gao, B. & Xu, X. 2020 Enhanced degradation of clothianidin in peroxymonosulfate/catalyst system via core-shell FeMn @ N-C and phosphate surrounding. *Applied Catalysis B: Environmental* **267**, 118717.

Fu, H., Ma, S., Zhao, P., Xu, S. & Zhan, S. 2019 Activation of peroxymonosulfate by graphitized hierarchical porous biochar and mnfe2o4 magnetic nanoarchitecture for organic pollutants degradation: structure dependence and mechanism. *Chemical Engineering Journal* **360**, 157–170.

Ghauch, A., Baalbaki, A., Amasha, M., El Asmar, R. & Tantawi, O. 2017 Contribution of persulfate in UV-254 nm activated systems for complete degradation of chloramphenicol antibiotic in water. *Chemical Engineering Journal* **317**, 1012–1025.

Gu, A., Wang, P., Chen, K., Miensah, E. D., Gong, C., Jiao, Y., Mao, P., Chen, K., Jiang, J., Liu, Y. & Yang, Y. 2022 Core-shell bimetallic Fe-Co MOFs to activated peroxymonosulfate for efficient degradation of 2-chlorophenol. *Separation and Purification Technology* **298**, 121461.

Guan, Y., Fu, G., Wang, Q., Ma, S., Yang, Y., Xin, B., Zhang, J., Wu, J. & Yao, T. 2022 Fe, Co, N co-doped hollow carbon capsules as a full pH range catalyst for pollutant degradation via a non-radical path in Fenton-like reaction. *Separation and Purification Technology* **299**, 121699.

Han, S. & Xiao, P. 2022 Catalytic degradation of tetracycline using peroxymonosulfate activated by cobalt and iron co-loaded pomelo peel biochar nanocomposite: characterization, performance and reaction mechanism. *Separation and Purification Technology* **287**, 120533.

Han, S., Xiao, P., An, L. & Wu, D. 2022a Oxidative degradation of tetracycline using peroxymonosulfate activated by cobalt-doped pomelo peel carbon composite. *Environmental Science and Pollution Research* **29** (15), 21656–21669.

Han, Y., Li, Z., Zhang, M., Han, F., Liu, Z. & Zhou, W. 2022b Isomorphic substitution of goethite by cobalt: effects on the pathway and performance of peroxymonosulfate activation. *Chemical Engineering Journal* **450**, 138460.

Hou, W., Huang, Y. & Liu, X. 2020 Highly efficient and recyclable ZIF-67 catalyst for the degradation of tetracycline. *Catalysis Letters* **150** (10), 3017–3022.

Hu, J., Zhang, J., Wang, Q., Ye, Q., Xu, H., Zhou, G. & Lu, J. 2019 Efficient degradation of tetracycline by ultraviolet-based activation of peroxymonosulfate and persulfate. *Water Science and Technology* **79** (5), 911–920.

Hu, Q., Cao, J., Yang, Z., Xiong, W., Xu, Z., Song, P., Jia, M., Zhang, Y., Peng, H. & Wu, A. 2021 Fabrication of Fe-doped cobalt zeolitic imidazolate framework derived from Co(OH)(2) for degradation of tetracycline via peroxymonosulfate activation. *Separation and Purification Technology* **259**, 118059.

Hu, L., Zhang, Y., Liu, X., Zhu, H., Wu, J., Wang, Y., Long, Y. & Fan, G. 2022 A robust peroxymonosulfate activator for tetracycline degradation: mitigating deactivation via stitching N-doped carbon nanotubes with encapsulated Co nanoparticles in bubble-like architectures. *Chemical Engineering Journal* **450**, 138219.

Hua, B., Zheng, L., Adeboye, A. & Li, F. 2022 Defect- and nitrogen-rich porous carbon embedded with Co NPs derived from self-assembled Co-ZIF-8 @ anionic polyacrylamide network as PMS activator for highly efficient removal of tetracycline hydrochloride from water. *Chemical Engineering Journal* **443**, 136439.

Jakob, M., Mahendran, A. R., Gindl-Altmutter, W., Bliem, P., Konnerth, J., Mueller, U. & Veigel, S. 2022 The strength and stiffness of oriented wood and cellulose-fibre materials: a review. Progress in Materials Science **125**, 100916.

Jin, X., Huang, Y., He, S., Chen, G., Liu, X., He, C., Du, C. & Chen, Q. 2023 Preparation of Co-Fe based Prussian blue analogs loaded nickel foams for Fenton-like degradation of tetracycline. *Applied Catalysis A: General* **650**, 118985.

Johar, N., Ahmad, I. & Dufresne, A. 2012 Extraction, preparation and characterization of cellulose fibres and nanocrystals from rice husk. *Industrial Crops and Products* **37** (1), 93–99.

Kang, J., Zhang, H., Duan, X., Sun, H., Tan, X., Liu, S. & Wang, S. 2019 Magnetic Ni-Co alloy encapsulated N-doped carbon nanotubes for catalytic membrane degradation of emerging contaminants. *Chemical Engineering Journal* **362**, 251–261.

Lamaming, J., Saalah, S., Rajin, M., Ismail, N. M. & Yaser, A. Z. 2022 A review on bamboo as an adsorbent for removal of pollutants for wastewater treatment. *International Journal of Chemical Engineering* **2022**, 7218759.

Li, Q., Liu, J., Ren, Z., Wang, Z., Mao, F., Wu, H., Zhou, R. & Bu, Y. 2022a Catalytic degradation of antibiotic by Co nanoparticles encapsulated in nitrogen-doped nanocarbon derived from Co-MOF for promoted peroxymonosulfate activation. *Chemical Engineering Journal* **429**, 132269.

Li, X., Zhang, W., Liu, Z., Wang, S., Zhang, X., Xu, B., Yu, P., Xu, Y. & Sun, Y. 2022b Effective removal of tetracycline from water by catalytic peroxymonosulfate oxidation over Co@MoS2: catalytic performance and degradation mechanism. *Separation and Purification Technology* **294**, 121139.

Li, Z., Chen, C., Xie, H., Yao, Y., Zhang, X., Brozena, A., Li, J., Ding, Y., Zhao, X., Hong, M., Qiao, H., Smith, L. M., Pan, X., Briber, R., Shi, S. Q. & Hu, L. 2022c Sustainable high-strength macrofibres extracted from natural bamboo. *Nature Sustainability* **5** (3), 235.

Li, C., Li, J., Huang, N., Kong, X. Y., Xiao, Q., Huang, Y., Wong, P. K. & Ye, L. 2023a Ultrastable Co-NC membrane for sterilization of Escherichia coli in flowing water. *Npj Clean Water* **6** (1), 47.

Li, Q., Ren, Z., Liu, Y., Zhang, C., Liu, J., Zhou, R., Bu, Y., Mao, F. & Wu, H. 2023b Petal-like hierarchical co3o4/N-doped porous carbon derived from Co-MOF for enhanced peroxymonosulfate activation to remove tetracycline hydrochloride. *Chemical Engineering Journal* **452**, 139545.

Liao, H., Liu, C., Zhong, J. & Li, J. 2022 Fabrication of BiOCl with adjustable oxygen vacancies and greatly elevated photocatalytic activity by using bamboo fiber surface embellishment. *Colloids and Surfaces A-Physicochemical and Engineering Aspects* **634**, 127892.

Liu, Z., Yang, S., Yuan, Y., Xu, J., Zhu, Y., Li, J. & Wu, F. 2017 A novel heterogeneous system for sulfate radical generation through sulfite activation on a cofe2o4 nanocatalyst surface. *Journal of Hazardous materials* **324**, 583–592.

Liu, Y., Chen, X., Yang, Y., Feng, Y., Wu, D. & Mao, S. 2019 Activation of persulfate with metal-organic framework-derived nitrogen-doped porous Co@C nanoboxes for highly efficient p-Chloroaniline removal. *Chemical Engineering Journal* **358**, 408–418.

Liu, J., Luo, K., Li, X., Yang, Q., Wang, D., Wu, Y., Chen, Z., Huang, X., Pi, Z., Du, W. & Guan, Z. 2020a The biochar-supported iron-copper bimetallic composite activating oxygen system for simultaneous adsorption and degradation of tetracycline. *Chemical Engineering Journal* **402**, 126039.

Liu, L., Li, Y., Li, W., Zhong, R., Lan, Y. & Guo, J. 2020b The efficient degradation of sulfisoxazole by singlet oxygen (O-1(2)) derived from activated peroxymonosulfate (PMS) with Co3O4-SnO2/RSBC. *Environmental Research* **187**, 109665.

Liu, T., Cui, K., Chen, Y., Li, C., Cui, M., Yao, H., Chen, Y. & Wang, S. 2021 Removal of chlorophenols in the aquatic environment by activation of peroxymonosulfate with nMnOx@Biochar hybrid composites: performance and mechanism. *Chemosphere* **283**, 131188.

Long, Y., Li, S., Yang, P., Chen, X., Liu, W., Zhan, X., Xue, C., Liu, D. & Huang, W. 2022 Synthesis of ZIF-67 derived honeycomb porous Co/NC catalyst for AO7 degradation via activation of peroxymonosulfate. *Separation and Purification Technology* **286**, 120470.

Luo, J., Bo, S., An, Q., Xiao, Z., Wang, H., Cai, W., Zhai, S. & Li, Z. 2020 Designing ordered composites with confined Co-N/C layers for efficient pollutant degradation: structure-dependent performance and PMS activation mechanism. *Microporous and Mesoporous Materials* **293**, 109810.

Luo, H., Sheng, B., Chen, X., Wang, Y., Chen, Q. & Zhou, J. 2021 Cu2 + /Cu+ cycle promoted PMS decomposition with the assistance of Mo for the degradation of organic pollutant. *Journal of Hazardous Materials* **411**, 125050.

Lv, C., Shi, J., Tang, Q. & Hu, Q. 2020 Tetracycline removal by activating persulfate with diatomite loading of Fe and Ce. *Molecules (Basel, Switzerland)* **25** (23), 5531.

Pang, G., Ji, M., Li, Z., Yang, Z., Qiu, X. & Zhao, Y. 2022 Electrospinning of ZIF-67 derived Co-C-N composite efficiently activating peroxymonosulfate to degrade dimethyl phthalate. *Water-Sui* **14** (14), 2248.

Peng, L., Duan, X., Shang, Y., Gao, B. & Xu, X. 2021 Engineered carbon supported single iron atom sites and iron clusters from Fe-rich Enteromorpha for Fenton-like reactions via nonradical pathways. *Applied Catalysis B: Environmental* **287**, 119963.

Qi, Y., Li, J., Zhang, Y., Cao, Q., Si, Y., Wu, Z., Akram, M. & Xu, X. 2021 Novel lignin-based single atom catalysts as peroxymonosulfate activator for pollutants degradation: role of single cobalt and electron transfer pathway. *Applied Catalysis B: Environmental* **286**, 119910.

Rasheed, M., Jawaid, M., Parveez, B., Zuriyati, A. & Khan, A. 2020 Morphological, chemical and thermal analysis of cellulose nanocrystals extracted from bamboo fibre. *International Journal of Biological Macromolecules* **160**, 183–191.

Song, Z., Zhang, X., Liu, B., Liu, J. & Wang, L. 2023 Efficient degradation of tetracycline residues in pharmaceutical wastewater by Ni/Fe bimetallic atomic cluster composite catalysts with enhanced electron transfer pathway. *Chemosphere* **335**, 139181.

Thanh-Binh, N., Huang, C. P., Doong, R.-a., Wang, M.-H., Chen, C.-W. & Dong, C.-D. 2022 Manipulating the morphology of 3D flower-like comn2o4 bimetallic catalyst for enhancing the activation of peroxymonosulfate toward the degradation of selected persistent pharmaceuticals in water. *Chemical Engineering Journal* **436**, 135244.

Wang, H., Yuan, X., Wu, Y., Zeng, G., Dong, H., Chen, X., Leng, L., Wu, Z. & Peng, L. 2016 In situ synthesis of in2S3@MIL-125(Ti) core-shell microparticle for the removal of tetracycline from wastewater by integrated adsorption and visible-light-driven photocatalysis. *Applied Catalysis B: Environmental* **186**, 19–29.

Wang, J., Jiang, Y., Gao, C., Li, Y. & Wu, X. 2021a Synergistic effect of bimetal in three-dimensional hierarchical mnco2o4 for high efficiency of photoinduced Fenton-like reaction. *Surf Interfaces* **27**, 101482.

Wang, T., Liu, X., Ma, C., Wei, M., Huo, P. & Yan, Y. 2021b In situconstruction of BiVO4(-)cellulose fibers@CDs(-)polyvinyl alcohol composites for tetracycline photocatalytic degradation. *Science China-Technological Sciences* **64** (3), 548–558.

Wang, W., Liang, M., Jiang, Y., Liao, C., Long, Q., Lai, X. & Liao, L. 2021c Nano-Co embedded in porous ZIF-67 polyhedron to catalyze hydrolysis of ammonia borane. *Materials Letters* **293**, 169702.

Wang, K., Guo, Y., Chen, Z., Wu, D., Zhang, S., Yang, B. & Zhang, J. 2022a Regulating electronic structure of two-dimensional porous Ni/Ni3N nanosheets architecture by Co atomic incorporation boosts alkaline water splitting. *Infomat* **4** (6), e12251.

Wang, W., Song, F., Du, C. & Su, Y. 2022b Durable and eco-friendly peroxymonosulfate activation over cobalt/tin oxides-based heterostructures for antibiotics removal: insight to mechanism, degradation pathway. *Journal of Colloid and Interface Science* **625**, 479–492.

Wu, Y., Li, Y., Zhao, T., Wang, X., Isaeva, V. I., Kustov, L. M., Yao, J. & Gao, J. 2022 Bimetal-organic framework-derived nanotube@cellulose aerogels for peroxymonosulfate (PMS) activation. *Carbohydrate Polymers* **296**, 119969.

Xie, J., Luo, X., Chen, L., Gong, X., Zhang, L. & Tian, J. 2022 ZIF-8 derived boron, nitrogen co-doped porous carbon as metal-free peroxymonosulfate activator for tetracycline hydrochloride degradation: performance, mechanism and biotoxicity. *Chemical Engineering Journal* **440**, 135760.

Xiong, M., Sun, Y., Chai, B., Fan, G. & Song, G. 2023 Efficient peroxymonosulfate activation by magnetic cofe2o4 nanoparticle immobilized on biochar toward sulfamethoxazole degradation: performance, mechanism and pathway. *Applications of Surface Science* **615**, 156398.

Xu, M., Deng, J., Cai, A., Ma, X., Li, J., Li, Q. & Li, X. 2020 Comparison of UVC and UVC/persulfate processes for tetracycline removal in water. *Chemical Engineering Journal* **384**, 123320.

Xu, C., Liu, Q., Wei, M., Guo, S., Fang, Y., Ni, Z., Yang, X., Zhang, S. & Qiu, R. 2022 Co@CoO encapsulated with N-doped carbon nanotubes activated peroxymonosulfate for efficient purification of organic wastewater. *Separation and Purification Technology* **295**, 121347.

Xue, K., Mo, Y., Long, B., Wei, W., Shan, C., Guo, S. & Niu, L. 2022 Single-atom catalysts supported on ordered porous materials: synthetic strategies and applications. *Infomat* **4** (6), e12296.

Yang, Y.-Y., Zhao, J.-L., Liu, Y.-S., Liu, W.-R., Zhang, Q.-Q., Yao, L., Hu, L.-X., Zhang, J.-N., Jiang, Y.-X. & Ying, G.-G. 2018 Pharmaceuticals and personal care products (PPCPs) and artificial sweeteners (ASs) in surface and ground waters and their application as indication of wastewater contamination. *Science of the Total Environment* **616**, 816–823.

Yang, G., Li, Y., Yang, S., Liao, J., Cai, X., Gao, Q., Fang, Y., Peng, F. & Zhang, S. 2021 Surface oxidized nano-cobalt wrapped by nitrogen-doped carbon nanotubes for efficient purification of organic wastewater. *Separation and Purification Technology* **259**, 118098.

Yao, C., Qin, Y., Li, Y., An, Q., Xiao, Z., Wang, C. & Zhai, S. 2023 Activation of peroxymonosulfate by cobalt-embedded carbon aerogels: preparation and singlet oxygen-dominated catalytic degradation insight. *Separation and Purification Technology* **307**, 122728.

Ye, S., Zeng, G., Tan, X., Wu, H., Liang, J., Song, B., Tang, N., Zhang, P., Yang, Y., Chen, Q. & Li, X. 2020 Nitrogen-doped biochar fiber with graphitization from Boehmeria nivea for promoted peroxymonosulfate activation and non-radical degradation pathways with enhancing electron transfer. *Applied Catalysis B: Environmental* **269**, 118850.

Zhang, X., Xu, B., Wang, S., Li, X., Wang, C., Liu, B., Han, F., Xu, Y., Yu, P. & Sun, Y. 2022a Tetracycline degradation by peroxymonosulfate activated with CoNx active sites: performance and activation mechanism. *Chemical Engineering Journal* **431**, 133477.

Zhang, X., Xue, D., Jiang, S., Xia, H., Yang, Y., Yan, W., Hu, J. & Zhang, J. 2022b Rational confinement engineering of MOF-derived carbon-based electrocatalysts toward CO2 reduction and O-2 reduction reactions. *Infomat* **4** (3), e12201.

Zhang, X., Zhang, H., Yu, J., Wu, Z. & Zhou, Q. 2022c Preparation of flower-like Co3O4 QDs/Bi2WO6 p-n heterojunction photocatalyst and its degradation mechanism of efficient visible-light-driven photocatalytic tetracycline antibiotics. *Applications of Surface Science* **585**, 152547.

Zhao, Z., Nie, T. & Zhou, W. 2019 Enhanced biochar stabilities and adsorption properties for tetracycline by synthesizing silica-composited biochar. *Environmental Pollution* **254**, 113015.

Zhao, H., Li, X., Zhang, L., Hu, Z., Zhong, L. & Xue, J. 2021 Preparation and bacteriostatic research of porous polyvinyl alcohol/biochar/nanosilver polymer gel for drinking water treatment. *Scientific Reports* **11** (1), 12205.

Zhao, X., Li, X., Zhu, Z., Hu, W., Zhang, H., Xu, J., Hu, X., Zhou, Y., Xu, M., Zhang, H. & Hu, G. 2022 Single-atom Co embedded in BCN matrix to achieve 100% conversion of peroxymonosulfate into singlet oxygen. *Applied Catalysis B-Environmental* **300**, 120759.

Zhong, Q., Lin, Q., Huang, R., Fu, H., Zhang, X., Luo, H. & Xiao, R. 2020 Oxidative degradation of tetracycline using persulfate activated by N and Cu codoped biochar. *Chemical Engineering Journal* **380**, 122608.

Zhu, H., Guo, A., Wang, S., Long, Y., Fan, G. & Yu, X. 2022 Efficient tetracycline degradation via peroxymonosulfate activation by magnetic Co/N co-doped biochar: emphasizing the important role of biochar graphitization. *Chemical Engineering Journal* **450**, 138428.

First received 20 June 2023; accepted in revised form 15 September 2023. Available online 6 October 2023